The Pennsylvania State University

The Graduate School

College of Engineering

# NEUTRON THERMALIZATION LIGHT YIELD MEASUREMENT

# VIA TIME-OF-FLIGHT TECHNIQUE IN EJ-290 SCINTILLATOR

A Thesis in

Nuclear Engineering

by

Tan Shi

Submitted in Partial Fulfillment

of the Requirements

for the Degree of

Master of Science

May 2016

The thesis of Tan Shi was reviewed and approved* by the following:

Igor Jovanovic
Professor of Nuclear Engineering
Thesis Advisor

Marek Flaska
Assistant Professor of Nuclear Engineering

Arthur Motta
Professor of Nuclear Engineering and Materials Science and Engineering
Chair of Nuclear Engineering

*Signatures are on file in the Graduate School.

# Abstract

Capture-gated neutron detection technique has shown great promise in neutron spectroscopy due to the preference for near-complete energy deposition prior to neutron capture and the resulting reduced continuum in the detector response functions. The dependence of light output of the polyvinyl toluene (PVT) scintillator EJ-290 on neutron energy is presented. Neutrons are detected with a recently developed heterogeneous composite scintillator based on EJ-290 scintillating PVT and $^6$Li-doped scintillating glass (GS20) rods. Besides the excellent pulse shape discrimination performance resulting from different decay times of the EJ-290 and GS20, the capability of both thermal neutron detection and fast neutron spectroscopy in a single detector makes the composite scintillator design attractive for a variety of applications. In this work, the nonproportional dependence of the scintillation light output of EJ-290 on deposited neutron energy has been measured in the range of 0–14.1 MeV through a combination of time-of-flight (TOF) measurement and previously conducted measurements with monoenergetic neutron sources (DD, 2.45 MeV and DT, 14.1 MeV). The TOF measurements were performed by tagging fission events occurring in a $^{252}$Cf spontaneous fission source over a period of 120 hours. The thermalization light output spectrum exhibits a more peak-like shape compared to non-capture-gated scintillation detector because of the nearly full energy deposition prior to neutron capture. The light output nonlinearity of the EJ-290 PVT resulting from energy-dependent quenching is described via the Birks and Chou parametrization, both of which produce good fits to experimental results. Geant4 simulation has also been used to simulate detector response to neutrons, which is helpful for understanding neutron interaction physics and for future detector optimization.

# Table of Contents

# List of Figures

# List of Tables

# List of Symbols

# Acknowledgments

First, I would like to express my greatest gratitude to Prof. Igor Jovanovic for his continuous guidance and mentoring as my thesis advisor in the completion of this study. I am especially thankful for his patient explanations, valuable guidance on the project and for his help in thesis writing. I also would like to show my deepest appreciation to Dr. Michael Mayer and graduate student Jason Nattress for their support in both experiments and simulations. My thesis study would not be possible without their effort and contributions to the project. I would like to thank Prof. Zoubeida Ounaies, Albert Foster, and Dr. Amira Meddeb for their help in detector material fabrication, and Prof. Kenan Unlu for providing EJ-309 detectors for TOF measurements. I would like to sincerely thank group members Dr. Ming-wei Lin and Kyle Hartig for valuable discussions. Last but not least, I would like to express my gratitude to Prof. Marek Flaska and Prof. Arthur Motta for reviewing this thesis and for providing candid advice to my thesis work.

# Chapter 1
# Introduction

## 1.1 Background and Motivation

Neutron detection finds its versatile applications in various disciplines including basic research [1, 2], health physics [3], radiation dosimetry [4], as well as nuclear security and safeguards [5]. Research in neutron detection has been of significant interest in the last few decades. There is ongoing effort to improve the reliability of neutron counting [6], perform neutron source identification and source imaging [7], as well as to improve the performance of neutron spectroscopy [8]. The $^3$He proportional counter has proven to be an benchmark neutron detector due to its superior neutron capture efficiency and low sensitivity to gamma rays. However, the shortage of $^3$He, caused by the limited supply from the nuclear weapon industries and the competing demands from other fields, continues to motivate the search for alternative neutron detection technologies [9, 10].

Major neutron detection techniques can be categorized based on the neutron energy and the detector operating principle. First, the neutron detection methods typically pertain to slow or fast neutrons. Slow neutron detection is defined as the detection of neutron with energy below the cadmium neutron cutoff of $\sim$0.5 eV [11]. Since neutrons carry no electric charge, slow neutrons are typically detected by observing the charged particles such as protons or alpha particles that are produced in neutron capture reactions. Common slow neutron detectors include the $^3$He proportional counter [12], $BF_3$ and boron-lined proportional counters [13] and lithium-loaded scintillators [14]. Fast neutron detection technique is quite different from slow neutron detection because of the reduced neutron capture reaction cross section. There is frequently an additional motivation to measure the fast neutron energy. Fast neutrons can be first moderated in an moderating material

and then detected via neutron capture reactions. Measurement devices based on this technique include the Bonner sphere spectrometer [15], spherical neutron dosimeter [16], etc. Fast neutrons can also be detected directly via fast neutron capture reactions, but the efficiency of this approach is low due to low cross sections at higher neutron energies [17]. Elastic scattering on light nuclei such as hydrogen is also common for fast neutron detection, where the energy deposited by the nuclear recoil can provide information about the incident neutron energy as well. Detectors based on this technique are referred to as proton recoil detectors, such as proton recoil scintillators [18], gas recoil proportional counters [19], and capture-gated neutron spectrometers [20].

The neutron detection in a lithium-doped composite scintillator described in this work relies on the $^6$Li(n,t)$^4$He neutron capture reaction. The detector is made of $^6$Li-doped glass rods (GS20) embedded into a polyvinyl toluene (PVT) scintillator EJ-290. While neutrons can be captured by the $^6$Li-doped glass rods and thus indicate the particle type based on both the reaction Q-value and scintillation pulse shape, neutron thermalization inside the PVT can be used to measure the neutron energy. This is done by measuring the scintillation pulse produced in PVT that immediately precedes the neutron capture event. One of the motivations for the composite detector prototype development is for the nuclear safeguards and the identification of special nuclear materials. Based on the previous results on the detector characterization, the detector exhibits excellent neutron/gamma discrimination [21]. Combined with the ability to perform neutron spectroscopy, the multiple functions within a single detector make the detector appealing in both passive and active measurements in nuclear security. In this work, the neutron spectroscopy performance of the constructed composite scintillator prototype detector was characterized through the capture-gated coincidence technique via the time-of-flight (TOF) measurement. Initial investigations of detector response have also been performed using Geant4 Monte Carlo simulations. Since the spectroscopy is based on the capture-gated technique, a brief introduction of this technique and the related previous works are provided in the next section.

## 1.2 Principle of Capture-Gated Detection

For capture-gated neutron detection, the detector is usually loaded with $^{10}$B, $^6$Li, or other nuclides such as $^{157}$Gd that have a large cross section for neutron capture. The $^{10}$B-loaded and $^6$Li-loaded neutron detector are the two most popular choices used for capture agents. The energy-dependent neutron capture cross section is shown in Fig. 1.1. The neutron capture on $^{10}$B has two reaction branches with $^7$Li at either ground state or excited state:

$$^{10}\text{B} + \text{n} \quad \rightarrow \quad ^7\text{Li}^\star(0.84 \text{ MeV}) + \alpha(1.47 \text{ MeV}) \quad \text{branching ratio: } 93.7\% \quad (1.1)$$

$$^7\text{Li}^\star \quad \rightarrow \quad ^7\text{Li} + \gamma(0.477 \text{ MeV}) \quad (1.2)$$

$$^{10}\text{B} + \text{n} \quad \rightarrow \quad ^7\text{Li}(1.01 \text{ MeV}) + \alpha(1.78 \text{ MeV}) \quad \text{branching ratio: } 6.3\% \quad (1.3)$$

The neutron capture on $^6$Li follows the reaction:

$$^6\text{Li} + \text{n} \rightarrow \text{t}(2.05 \text{ MeV}) + \alpha(2.73 \text{ MeV}) \quad (1.4)$$
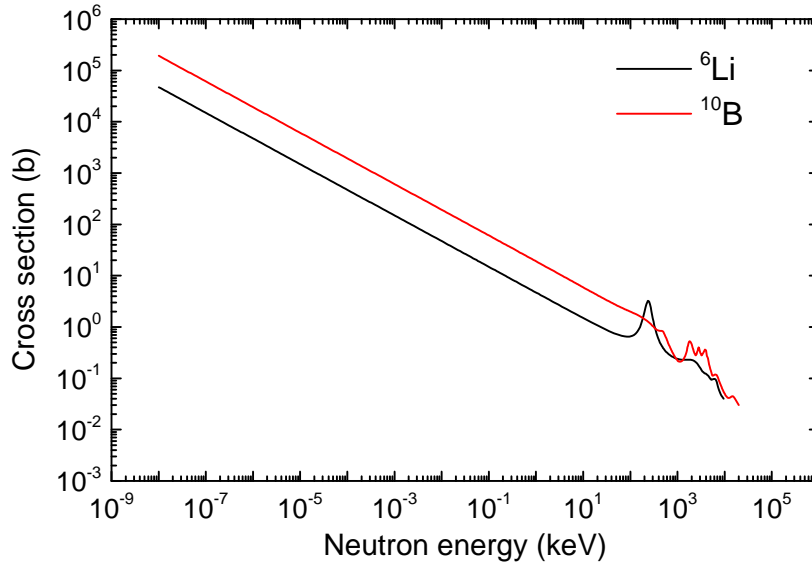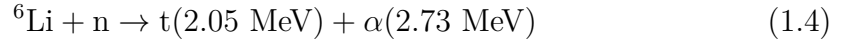


**Figure 1.1.** $^6$Li and $^{10}$B neutron capture cross section as a function of neutron energy. The data have been obtained from JEFF-3.1 nuclear data library [17].

Prior to the neutron capture reaction such as $^6$Li(n,t)$^4$He or $^{10}$B(n,$\alpha$)$^7$Li, the neutron is usually thermalized in the surrounding detector medium. In the thermal-

ization process, multiple neutron scatters can take place in rapid succession. The aggregate light output from these multiple scatters is measured using a sensitive light detection devices such as a photomultiplier tube. A single light pulse is observed from a combination of all scatters, referred to as a thermalization pulse or scattering pulse. The terms *thermalization pulse* and *scattering pulse* are used interchangeably in this work. The terms *start pulse* [22] or *first pulse* [23] have been used in the literature as well, since the neutron thermalization precedes the neutron capture. It is noteworthy that although the use of the term *thermalization pulse* implies full neutron thermalization, only a fraction of the neutrons are fully thermalized prior to their capture. After the neutron has lost most of its energy through multiple scatters, it diffuses within the scintillator until it is captured by $^{10}$B and $^{6}$Li, or escapes from the detector.
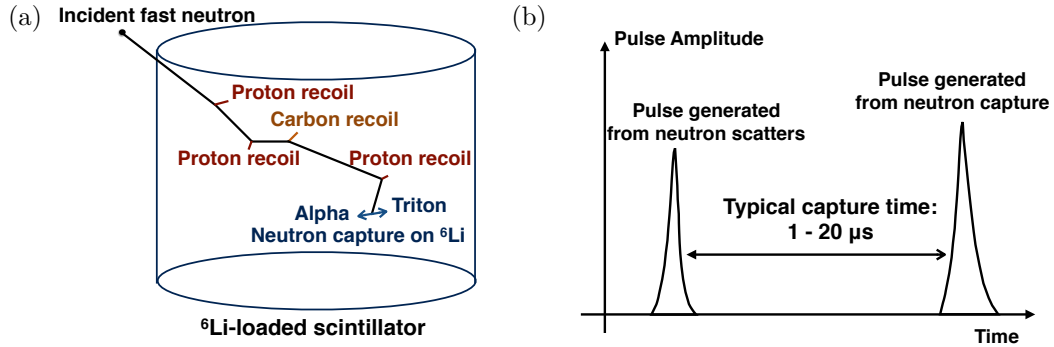


**Figure 1.2.** (a) Illustration of the principle of the capture-gated detection (b) Scatter pulse and capture pulse from a capture-gated neutron detector, image reproduced based on [24].

Therefore, the signature of the detection of fast neutron in the composite detector studied in this work usually consists of two correlated pulses. The first pulse is generated by neutron scattering, while the second pulse is generated by neutron capture, as shown in Fig. 1.2. The time difference between the two pulses (referred to as the capture time) is typically 1–20 µs, and it depends on the detector composition and geometry. Since the thermalization pulse is time-correlated to the capture pulse, the thermalization pulse light output is highly correlated to the neutron energy because most of the neutron energy is lost before the capture. Because of this preference for near-complete energy deposition, capture-gated detector produces a pulse height or pulse area spectrum that exhibits a peak-like

feature for monoenergetic neutrons. However, due to a variety of thermalization histories, the nonproportionality of organic scintillators [25, 26] and other statistical and electronics uncertainties, the light output is not always the same even though the same amount of energy is deposited in the detector. Both proton and carbon nuclei, which produce different light yields, are involved in the scatter process. Depending on the scatter collision sequence, the types of recoils and the energies of the recoils, the total light output departs from an ideal peak for monoenergetic neutrons. Nevertheless, the strong correlation of the light output to incident neutron energy still makes capture-gated detectors useful for spectroscopic applications. While the capture-gated technique has been investigated for various detector types in the past, efforts are still being made to develop novel detector structures with improved performance [14, 27].

## 1.3 Previous Work on Capture-Gated Detection

Fast neutron detection via capture-gated technique has been studied in multiple works with both $^6$Li-loaded and $^{10}$B-loaded scintillators, as well as with other detector configurations. A non-exhaustive list of the previous research is provided in this chapter in Table 1.1. in chronological order.

Although these studies involved different types of capture-gated detectors, the principle of the measurement is common with the work presented here. A review of the previous research in this area helps to better understand the scope of the current work. It is noted that only a fraction of the studies presented in Table 1.1 have discussed the spectroscopic capability of detectors used or have performed their spectroscopic characterization. In addition, in some works involving capture-gated detection, the term *neutron coincidence spectrometer* was used [20]. As these previous works are summarized in this chapter, particular focus is made on the detector design and configuration, detector characteristics (such as capture time and intrinsic efficiency), spectroscopic response, spectral reconstruction scheme, as well as suitable applications.

The work of Feldman *et al.* was motivated by space tests at that time, *e.g.* the measurement of fast neutron flux in near-earth space in the presence of significant cosmic ray background [28]. The detection system consisted of four PVT-based plastic scintillators loaded with 5% natural boron in weight. The mean capture

| Authors and year | Detector type | Comments |
|---|---|---|
| Feldman *et al.*, 1991 [28] | $^{10}$B-loaded plastic scintillator BC-454 | Spectroscopic measurement from 0.6 MeV to 20 MeV, MCNP simulation, $^{252}$Cf spectrum reconstruction, space tests |
| Kamykowski *et al.*, 1992 [29] | $^{10}$B-loaded plastic scintillator BC-454 | Spectroscopic measurement, MCNP simulation |
| Aoyama *et al.*, 1993 [30] | $^{10}$B-loaded liquid scintillator BC-523 | Spectroscopic measurement using monoenergetic neutron source, MCNP simulation |
| Czirr *et al.*, 1994 [20] | Combined plastic scintillator BC-400 and $^6$Li-glass plates | Spectroscopic measurement using monoenergetic neutron source |
| Czirr *et al.*, 2002 [4], Flaska *et al.*, 2008 [31] | Lithium-gadolinium-borate (LGB) neutron detector | Detector design discussion, detector characterization, MCNP simulation |
| Abdurashitov *et al.*, 2002 [32] | Enriched $^6$Li-doped liquid scintillator | Detector design discussion |
| Jastaniah *et al.*, 2004 [23] | $^{10}$B-loaded liquid scintillator BC-523A | Detector pulse shape discrimination (PSD) characterization, capture-gated technique discussion |
| Pozzi *et al.*, 2005 [33] | $^{10}$B-loaded liquid scintillator BC-523A | MCNP simulation |
| Fisher *et al.*, 2011 [22] | $^6$Li-loaded liquid scintillator | Detector fabrication and characterization |
| Bass *et al.*, 2013 [14] | $^6$Li-loaded liquid scintillator | Thermal neutron measurement, spectroscopic measurement using monoenergetic neutron source, MCNP simulation |
| Holm *et al.*, 2014 [27] | $^{10}$B-loaded plastic scintillator | Detector fabrication and characterization |

**Table 1.1.** Previous work on capture-gated neutron detection technique.

time $\tau_0$ was estimated as [28]:

$$\tau_0 = (N_{^{10}B}\sigma v)^{-1} = 2.2 \ \mu s, \tag{1.5}$$

where $N_{^{10}B}$ is the number of $^{10}$B nuclide per unit volume, $\sigma$ is the neutron capture cross section of $^{10}$B and $v$ is the speed of neutron. This expression should be valid

for detector types where $^{10}$B or $^6$Li is homogeneously distributed in the detector. For inhomogeneous mixture of $^{10}$B or $^6$Li with scintillating materials, computational modeling is required to predict the capture time distribution. According to Feldman *et al.*, the neutron capture time distribution $P(t)$ can be expressed as [28]:

$$P(t) = \tau^{-1} \exp(-t/\tau), \tag{1.6}$$

where $\tau$ is the mean capture time. The distribution of time delay between the scattering pulse and the capture pulse was measured to compare with theoretical calculation. Based on the capture time distribution corrected for the chance coincidence rate, the measured mean capture time was calculated to be 2.4 µs, which was relatively close to the predicted mean capture time of 2.2 µs.

In the same work, Feldman *et al.* also measured and unfolded the $^{252}$Cf spectrum using an event-by-event reconstruction scheme. The calibration relationship between proton energy and light output was used to convert the measured light output to neutron energy. Since four detectors were used in the detection system, the light output from multiple detectors was summed to obtain the total incident neutron energy. However, when this event-by-event scheme was applied, one needs to assume that the light output from carbon recoil is negligible and that the light output is proportional to proton energy. Since multiple scattering events could take place in a single detector, the total light output of these multiple scattering events cannot be directly converted to proton energy. This is because the relationship between the light output ($L$) and the proton energy ($E$) is not linear: $L(E_1) + L(E_2) < L(E_1 + E_2)$ for protons with energies $E_1$ and $E_2$. The authors also acknowledged the limitation resulting from light output nonproportionality on the energy resolution of this unfolding scheme. However, the reconstructed $^{252}$Cf spectrum showed a good agreement with the known $^{252}$Cf neutron spectrum. Therefore, with certain assumptions made, this approach should be still applicable in some applications. Although spectroscopic measurement with monoenergetic neutron source was performed, it was not used to determine the response functions for two reasons: first, the non-negligible contribution of room scatter could not be easily removed; second, the high dead time operation of the detector under the stable operation of Van de Graaff accelerator was also an issue for obtaining reliable spectrum and accurate detector efficiency. The relationship between the detector

intrinsic efficiency and the incident neutron energy was therefore determined by Monte Carlo simulation using the MCNP package, and was in turn used to reconstruct the spectrum. After extensive characterization of the detection system, the detector was deployed in real space tests. The results obtained from measurements in space were also analyzed.

In the work of Kamykowski [29], the plastic detector BC-454 was loaded with 5% natural boron (resulting in approximately 1% fraction of $^{10}$B in the medium). The detector was studied in both ungated mode (as a normal proton recoil detector) and gated mode. For the capture-gated mode, the response to the neutron scatter was characterized using 4–7 MeV neutron. The neutrons were generated in the (d,d) reaction using a 4 MV Van de Graaff accelerator. The scintillating light output spectra for 4, 5, and 6 MeV neutrons were presented. Monte Carlo code MCNP (version 3A) was used to model the detector light output response. The conversion from recoil energy to light output was based on the published data on NE-213 liquid organic scintillator in which both the light output of carbon and hydrogen recoils were provided [18]. After data processing, including the removal of continuum in the measured spectrum induced by background and room scatter, energy gain adjustment, and real detector Gaussian smearing in simulated spectra, the measured and the modeled spectra showed good consistency. The measured spectra in general represented a peak-like feature while some of them had a shape of two non-resolved closely-positioned peaks (double lobed peak). Based on the MCNP results, the high energy end of the spectrum was explained by proton scattering events, which would result in significant light yield. The low energy part of the spectrum was explained by initial scatters on carbon since carbon recoil produced less light yield compared to proton recoil while significant incident neutron energy was lost in collisions with carbon. The intermediate part of the light output spectrum was attributed to multiple scatters involving both proton and carbon. Depending on the collision sequence, collision type, and energy deposition, the light output can vary and results in broadening of the response peak. Intrinsic efficiency and capture time distribution showed good agreement of measurement and simulation. Similar spectroscopic measurements and light output simulations were also performed in the work of Aoyama *et al.* for boron-loaded liquid scintillator BC-523 using 1.2 MeV, 2.4 MeV, 5 MeV, and 14.6 MeV neutron sources [30]. However, only light output of proton was taken into account by assuming negligible light yield from carbon. A

good agreement was found for neutron energies below 3 MeV, but not higher than 3 MeV. For example, the double peak feature at 5 MeV could not be obtained from the simulation result. Multiple possible causes for the discrepancy were discussed in the work, which would not be developed here [30].

The detector developed by Czirr *et al.* in 1994 was composed of four cylindrical BC-400 plastic scintillators vertically separated by $^6$Li-doped scintillating glass plates [20]. All the parts were enclosed in an aluminum housing and connected to one single photomultiplier (PMT) at one end. The detector design is relatively simple and can be considered as a stacking of two different scintillation materials with mineral oil added to the interface to assure optical coupling. Instead of the name capture-gated detector, neutron coincidence spectrometer was used. The scattering pulse (or thermalization pulse) light output was characterized using 1.2 MeV, 2.45 MeV, 4.5 MeV, 6.7 MeV and 14.1 MeV monoenergetic neutron source generated from (p,t), (d,d) and (d,t) reactions. An acceptance window of 20 µs was applied based on the mean capture time of 11 µs. It was found that even with low neutron flux, the chance coincidence rate was significant and more than one neutron scattering pulse candidate was frequently found within this time window due to the large mean capture time. These double scattering pulses were eliminated because plastic scintillator itself does not have PSD capability to identify the real scattering pulse. In order to obtain the light output response from a monoenergetic neutron source, shadow-shield technique was applied to account for room-scatter neutrons. However, low-energy neutrons from the neutron generator were not taken into account, which could partially explain the reason for noted inconsistency in background subtraction. After the background subtraction, the measured light output spectrum at 1.2 MeV could be described by one single broadened peak. At 2.45 MeV, a plateau was observed on the left side of the main peak. At 4.5 MeV and above, a double peak feature could be identified with one peak at low energy and one peak at high energy. It was suggested that the background neutron could be underestimated in some cases. However, the origin of the low energy peak and the shape of the spectrum was not discussed. Potential applications of this approach were described in this study, including radiation dosimetry and basic nuclear physics research.

The work by Czirr *et al.* in 2002 described the application of a lithium-gadolinium-borate neutron detector [4]. The main application is related to neutron

dosimetry and spectroscopy. The detector was made of plastic scintillator incorporating 5% $^6$Li$_6$Gd($^{11}$BO$_3$)$_3$:Ce borate crystal in weight. The pulse area spectrum and detector intrinsic efficiency were modeled by Monte Carlo simulation. A later study by Flaska *et al.* in 2008 [31] included LGB detector characterization. A detailed comparison between measured and simulated results was made, including capture time distribution and pulse height distribution of $^{252}$Cf source under various conditions. A good agreement could be observed from these results. The simulated pulse height distribution for monoenergetic neutrons (2, 4, 6, 8, 10 MeV) was also shown in this work.

In the work of Abdurashitov *et al.* in 2002, the possibility of designing an enriched $^6$Li-doped liquid scintillation spectrometer was discussed from a theoretical perspective. However, no real detector was fabricated or characterized [32]. The research on $^6$Li-loaded liquid scintillator characterization by Fisher *et al.* in 2011 was a continuation of the detector design work in 2002 [22]. The motivations for developing such a detector include applications in fundamental physics research, neutron measurement in space, as well as applications in health physics and radiation dosimetry. The stated goal was to achieve 5%–10% energy resolution for 14 MeV neutrons. Based on this goal, the design and construction of the spectrometer was discussed. The light output nonlinearity was considered as the major problem for the moderate energy resolution. The neutron moderation takes place in a very short time ($\tilde1$0 ns) so that it is difficult to obtain separate neutron scattering pulses. Thus, the authors proposed to divide the scintillator volume into several optically independent volumes. In this way, multiple neutron scatters have a very low probability to occur in the same segment of the detector. Each scattering pulse could be converted to light signal independently. A similar concept could be found in the work of Feldman *et al.*, where four boron-loaded scintillators were used to obtain the total light yield from one incident neutron [28].

In the work of Jastaniah *et al.*, the capture-gated technique was investigated based on the detector type of enriched $^{10}$B-loaded liquid scintillator (BC-523A) [23]. Even though the light output of neutron capture reaction was relatively low in the liquid scintillator BC-523A (about 60 keVee), the PSD capability of the BC-523A had the advantage of discriminating neutron scatter events from gamma events. Digital pulse processing techniques employing capture-gated trigger circuitry were described in this study. The time distribution between the neutron scattering

pulse and the capture pulse was also presented. Based on the mean capture time dependence on $^{10}$B concentration, it was shown that the higher $^{10}$B concentration of BC-523A detector had the benefit of reducing the mean neutron capture time, which resulted in a lower accidental coincidence rate. The neutron spectroscopic capability was suggested, but not fully characterized in this work.

The capture-gated detector response has also been modeled using Monte Carlo analysis by Pozzi *et al.* [33]. The detector type BC-523A, which had been characterized experimentally, was investigated using the code MCNP-PoliMi. The neutron collision sequence and the related time and energy deposition information were extracted from MCNP code, which served as the basis for the detector response analysis. For each interaction, the nonlinear relationship between the light output and the energy transferred from neutron to hydrogen was described via a second-order polynomial [33, 34]:

$$L = 0.0350E_n^2 + 0.1410E_n, \tag{1.7}$$

where $L$ is the light yield (in MeVee) and $E_n$ is the energy deposition from neutron to proton recoil. This relationship was obtained from measurements using liquid scintillator BC-501 and used for studying BC-523A response due to the lack of light output data for BC-523A in the literature. The light output of inelastic and elastic scattering with carbon, boron, and oxygen atoms were ignored because of the small light output. However, according to the work of Kamykowski [29], the light output of carbon is essential to explain certain features in the measured spectra. Based on the current assumption of negligible light yield of carbon recoil, total light output from one incident neutron was determined by summing up the light output of each interaction with proton. The response spectra for various incident neutron energies were obtained. The simulated spectrum for 5 MeV neutrons was further compared with experimental results from Aoyama *et al.*, showing good agreement. The average number of collisions before neutron capture, the neutron energy distribution immediately before neutron capture, the time to capture, the detector efficiency, as well as the comparison between detectors of different sizes were also presented in this work. Due to the complexity of capture-gated detection working principle, these simulation results are useful in interpreting the experimental results and in optimizing the detector design.

In the work of Bass *et al.* [14], a liquid scintillator loaded with 0.4% $^6$Li in weight was fabricated by incorporating lithium chloride solution into the Quickszint 164, a commercial scintillation cocktail that allows incorporation of aqueous solutions. The chemistry of lithium-loaded scintillator and the possible choice of lithium aqueous compounds were discussed. The dependence of optical transmittance on lithium chloride concentration was also taken into account during the detector fabrication. Based on the fluorescence measurement, the lithium-loaded detector showed decreased fluorescence intensity compared to pure scintillator without lithium incorporation. From this result, it is noteworthy that the material light output property would change during the process of the lithium compound addition, which should not be neglected in the simulation of light output. The detector was characterized by both thermal neutrons and fast neutrons, where 2.45 MeV, 14.1 MeV, and $^{252}$Cf source were used for fast neutron characterization. Monte Carlo simulation of the detector light output spectra was also performed and showed good agreement with measured thermalization pulse spectra. The Monte Carlo simulation took into account the geometry of the neutron source facility in which the room scatter resulted in the low energy tail in both the measured and simulated spectra. In the simulation, the light yield response of various charged particles (proton, carbon, etc.) was obtained from literature data on NE-213 liquid scintillator, which was also used in the work of Kamykowski *et al.* for the light output simulation [18] [29]. The discussion on detector efficiency, pulse shape discrimination technique, energy resolution and the comparison with boron-loaded detectors provided insights for the future lithium-loaded detector development. Besides the work of Bass *et al.*, $^6$Li-loaded liquid scintillator prototype was also developed by Fisher *et al.* [22]. Although extensive spectroscopic analysis was not studied in this work, investigations on PSD technique and shielded source characterization were performed.

In summary, a general trend can be seen from earlier research on commercial $^{10}$B-loaded scintillator characterization to more recent research on $^6$Li-loaded scintillator prototype development. The $^6$Li-loaded scintillator has the benefits of large Q-value (4.78 MeV) and increased light yield that allows neutron captures to be distinguished from background and low energy gamma ray depositions. Regarding the spectroscopic performance, the capture-gated detector exhibits a more peak-like response shape compared to non-gated proton recoil detector. Based on these

reasons, measurement and simulation were performed in this thesis to better understand the composite detector spectroscopic capability via the capture-gated technique.

# Chapter 2
# The $^{6}$Li-Doped Composite Scintillation Detector Prototype

## 2.1 Detector Geometry, Principle and Fabrication

The $^{6}$Li-doped composite scintillation detector prototype was designed and fabricated by Mayer *et al.* at Pennsylvania State University (Penn State). A detailed description of the detector geometry optimization, detector fabrication and performance characterization can be found in Refs. [21] and [35]. The measurements and simulation analysis presented here are all based on the same composite detector prototype. Therefore, a brief description of the detector geometry, operation principle and the previously measured detector response is given in this chapter.
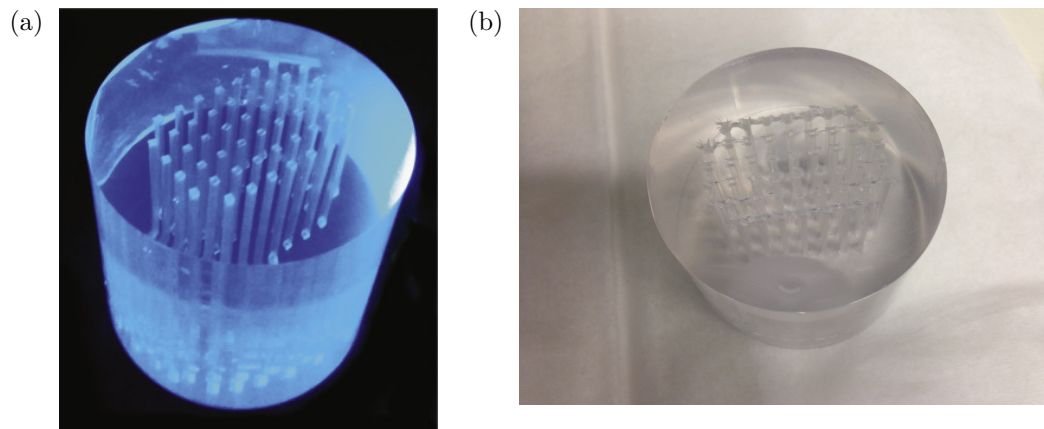


**Figure 2.1.** Fabricated $^{6}$Li-doped composite scintillation detector under (a) ultraviolet light exposure (image courtesy of Mayer *et al.*) and (b) fluorescent light exposure.

The fabricated detector has a cylinder shape with a height of 5.05 cm and a diameter of 5.08 cm. A total of fifty lithium-doped square rods are embedded in

the PVT polymer and arranged in the way as presented in Fig. 2.1. Each square rod has a cross sectional area of $1 \times 1$ mm$^2$ and has the same height as the detector (5.05 cm). The rods are composed of $^6$Li-enriched scintillating glass GS20 with 6.6% lithium oxide by weight. The glass rods are surrounded by the scintillating material EJ-290, which is a PVT-based partially polymerized resin. One advantage of EJ-290 polymer is its flexibility in fabricating heterogeneous detector. The major properties of GS20 glass and EJ-290 polymer are listed in Table 2.1.

| Properties | EJ-290 polymer | GS20 glass |
|---|---|---|
| Light output relative to anthracene | 60 % | 20 % - 30 % |
| Neutron excitation decay time (ns) | 2.4 (main component) | 18 (slow component); 57 (long component) |
| Wavelength of maximum emission (nm) | 423 | 395 |
| Density (g/cm$^3$) | 1.02 | 2.5 |
| Composition | H:C atomic ratio: 1.103 | Li$_2$O, SiO$_2$, Al$_2$O$_3$, MgO, etc.; isotopic ratio of $^6$Li in Li$_2$O: 95% |

**Table 2.1.** Properties of the GS20 glass and the EJ-290 polymer employed in the composite detector [36, 37].

The EJ-290 PVT polymer is mostly composed of hydrogen and carbon atoms, which have low mass and good neutron moderation capability. After a neutron is moderated in the PVT, it can be captured in the lithium-doped glass by the $^6$Li(n,t)$^4$He reaction shown in Eq. (1.4). After the released energy (Q-value) of the exothermic neutron capture reaction is imparted to the reaction products $^4$He (2.73 MeV) and $^3$H (2.05 MeV), a fraction of the particle kinetic energy is converted to light. The fraction of the energy converted to light depends on the particle stopping power, which is referred to as quenching. The quenching effect stems from the fact that along the path of the charged particle, the charged particle produces a local concentration of ionized molecules or so-called damaged molecules, which serve as quenching agents for the excitons produced by the ionizing particle [25]. In other words, the excitons do not only deexcite by means of fluorescence, but also via non-radiative recombination promoted by the damaged molecules, which reduce the

total light output. Nevertheless, the large Q-value from the $^6$Li(n,t)$^4$He reaction is still desirable because it leads to higher light output and is thus favorable for neutron capture/gamma discrimination. Furthermore, the different decay times of the two distinct materials used in the composite also lead to distinct PSD capability. Besides the PSD capability, the light output induced by neutron moderation, mostly inside the PVT, can be used to correlate to the incident neutron energy for fast neutron spectroscopy, as discussed in Chapter 1.

After the cylindrical detector was fabricated, it was optically coupled to the Hamamatsu R6231-100 PMT with optical grease covered evenly on both sides of the interface. In order to obtain high light collection efficiency, the detector and the PMT assembly were covered by a highly reflective paper-like material Tyvek, which consists of high density polyethylene. At the exterior of the Tyvek, the detector assembly was further wrapped by a layer of black Tedlar with the use of black electrical tape to maintain light isolation between the detector and the exterior environment. For the operation of the detector, the detector was connected to a digitizer and a high voltage power supply. The operating voltage of the PMT was approximately 1200 V.

## 2.2 Detector Response

The composite detector is sensitive to both gamma rays and neutrons. A typical gamma pulse and neutron capture pulse are shown in Fig. 2.2. Since the lithium-doped scintillating glass has a longer decay constant compared to PVT, the neutron capture pulse has a much larger tail and can therefore be distinguished by pulse shape analysis.

The pulse shape parameter (PSP) is used to quantify the shape of the pulse and is defined by

$$PSP = \frac{Pulse\ tail\ area}{Pulse\ total\ area} \tag{2.1}$$

where the pulse total area is obtained by integrating the entire waveform after the baseline subtraction, usually from 20 ns prior to the pulse peak to 160 ns after the pulse peak. The pulse tail area is obtained by integrating the tail region of the waveform, usually from 18 ns after the pulse peak to 160 ns after the pulse peak. These values were optimized to improve the PSD performance.

(a)



(b)
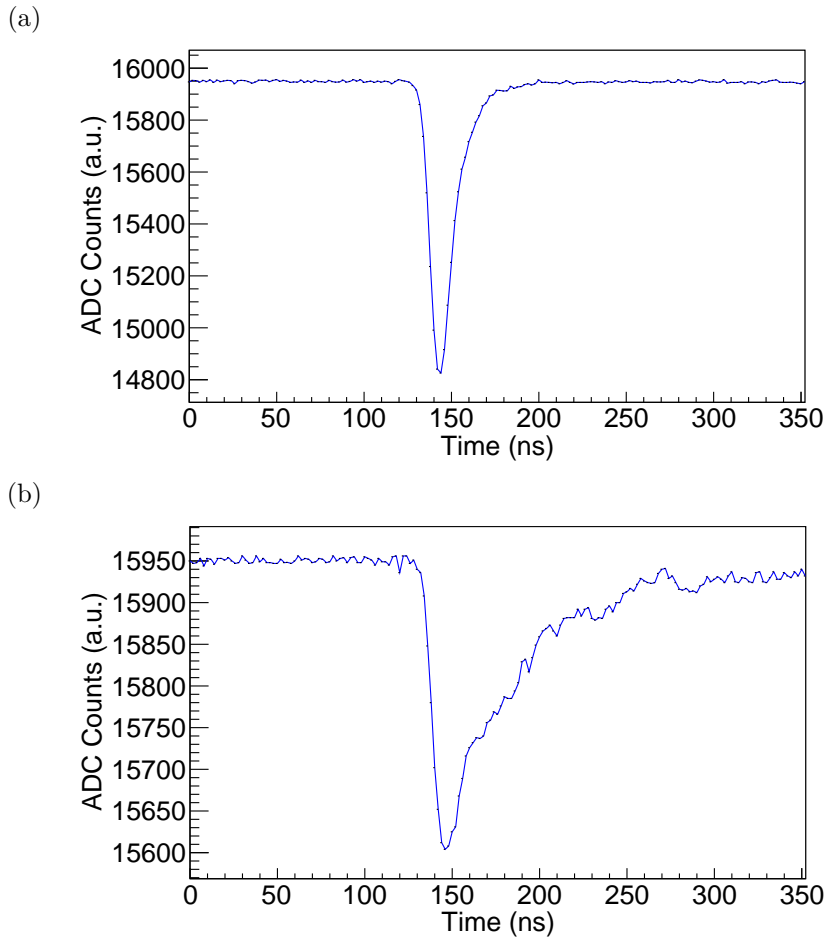


**Figure 2.2.** A typical waveform originating from (a) gamma event in the PVT and (b) neutron capture event in the $^6$Li-doped glass. The pulse amplitude is represented by arbitrary ADC counts output from the digitizer.

The PSD capability of the composite detector is demonstrated in Fig. 2.3 with the detector exposed to $^{252}$Cf spontaneous fission source, which emits both gamma rays and neutrons with a wide spectrum of energy. The circular region constrained by 0.4<PSP<0.8 is attributed to neutron capture events. They are clustered at approximately the same region because of the large Q-value of the reaction, the high capture probability of the thermalized and quasi-thermalized neutrons, as well as the distinct decay constant of the capture medium. The gamma events and the neutron thermalization events are located in the horizontal band at the bottom of the Fig. 2.3 (a). The gamma events have range of pulse amplitudes and areas because of continuous range of energy depositions, mostly by Compton scattering.
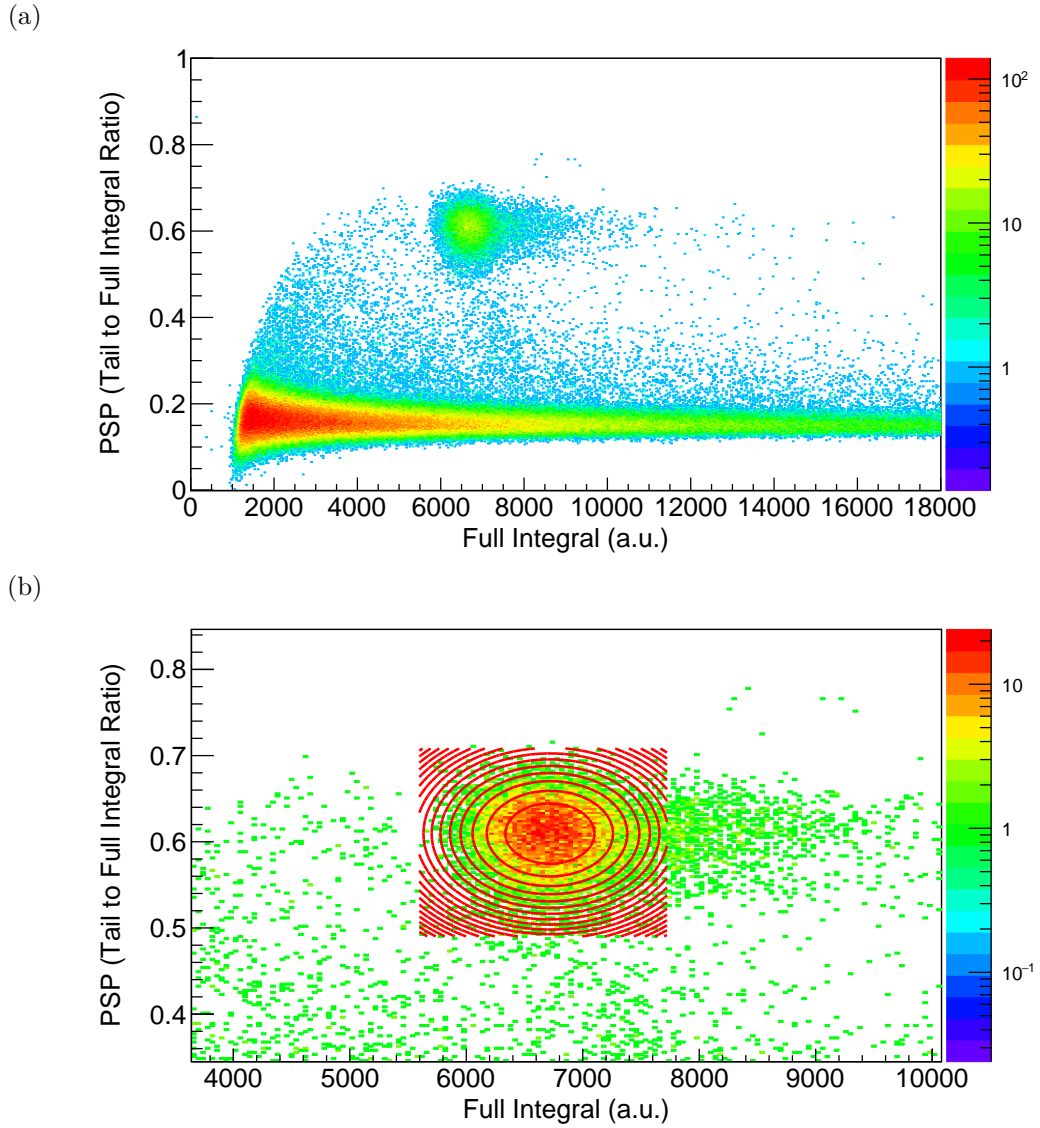
**Figure 2.3.** (a) Two-dimensional histogram of the PSP and the total pulse area (full integral) under the exposure of $^{252}$Cf source (b) Two-dimensional gaussian fit to the neutron capture region.

The neutron events are selected through a two-dimensional criterion based on a fit of a pulse to a combination of PSP and the total area. The events that lie within $3\,\sigma$ region of the fit are considered as real neutron capture events. The intrinsic neutron detection efficiency of the composite detector is $0.00337 \pm 0.00021$ for unshielded $^{252}$Cf spontaneous fission source [21]. The gamma rejection ratio of the detector was determined by measurement using $^{60}$Co gamma source. With the use

of both pulse shape analysis and pulse height analysis, the gamma rejection ratio was calculated to be less than $10^{-8}$ [21]. Besides the distinct PSD capability of the composite detector design, the potential of the detector for neutron spectroscopy is studied in Chapter 3 and Chapter 4.

# Chapter 3
# Neutron Spectroscopy Measurement

## 3.1  Experimental Method

The relationship between the light output from the EJ-290 scintillator and the incident neutron energy was characterized using TOF and monoenergetic neutron measurements, where the monoenergetic neutron measurements were performed by Nattress *et al.* [38] using 2.45 MeV and 14.1 MeV neutrons from DD and DT fusion reactions. The TOF measurements were performed at the Penn State Materials Research Institute by tagging the fission events produced in a $^{252}$Cf source over a period of 120 hours. The $^{252}$Cf source has a Watt fission spectrum which peaks at 0.8 MeV with an average energy of 2.1 MeV [39]. Each spontaneous fission event emits on average 10 gamma rays and 3.8 neutrons. Prompt gammas and neutrons are emitted nearly simultaneously, so that the time of the fission event can be tagged using gamma rays, while the energy of neutrons detected in the composite detector can be determined from the neutron TOF. Fission events are tagged by positioning detectors closely to the $^{252}$Cf source in order to obtain a high tagging efficiency. After the TOF is determined, the energy of the incident neutron $E_{neutron}$ can be calculated by

$$E_{neutron} = \frac{m_{neutron}}{2} \left( \frac{Distance}{TOF} \right)^2.$$  (3.1)

The composite detector needs to be placed a certain distance away from the source. Those choice of distance represents a trade-off between the neutron capture efficiency and the energy resolution. By tagging the fission event, the light output of the thermalization pulse can therefore be correlated to the incident neutron energy even without the use of a monoenergetic neutron source.

The experimental setup and the equipment for the TOF measurement are presented in Fig. 3.1 and Table 3.1.

| Equipment | Manufacturer | Model | Specifications |
|---|---|---|---|
| High voltage power supply | CAEN | DT5533 | 4 channels, desktop module, maximum output voltage: 4 kV |
| Digitizer | CAEN | DT5730 | 8 channels, desktop module, 14-bit at 500 MS/s |
| Delay generator | SRS | SRS DG645 | 4 pulse, 8 delay outputs, Trigger rates to 10 MHz |
| Three liquid scintillators | ELJEN | EJ-309 | Decay Time (short component): 3.5 ns, PSD capability |
| Computer | Dell | – | – |
| Radioactive sources: $^{252}$Cf, $^{137}$Cs, $^{60}$Co | – | – | Activity $^{252}$Cf: 662 µCi; $^{60}$Co: 0.28 µCi; $^{137}$Cs: 4.7 µCi |

**Table 3.1.** Equipment for the TOF measurement.

In the measurement, three calibrated EJ-309 liquid scintillation detectors were placed 5 cm away from the $^{252}$Cf source. Gamma events detected in the EJ-309 detectors and selected by use of the EJ-309 PSD properties were used as the start signal for a fission event. The composite detector was placed 1.6 m away from the source and 1 m above the concrete laboratory floor. Events within the TOF acceptance window of 50 ns<TOF<410 ns were selected as potential neutron thermalization pulse candidates from the composite detector, corresponding to incident neutron energies $E_n$ of 5 MeV> $E_n$ >80 keV. The thermalization pulse cannot be distinguished only on the basis of pulse shape, since both the gamma rays and neutrons interact with the EJ-290 scintillator, which does not exhibit PSD. The neutron capture pulses were identified through a two-dimensional Gaussian fit, as explained previously in Chapter 2. Only the events that lie within the $3\sigma$ region of the neutron peak area were selected as neutron capture events. Simulations of the composite detector conducted using the Geant4 Monte Carlo code [40] reveal the mean neutron thermalization-to-capture (diffusion) time of 2.67 µs, with >99% of the capture events having a diffusion time <50 µs [38]. Therefore, an inter-event timing gate of 50 µs, along with the pulse shape consistent with the event taking
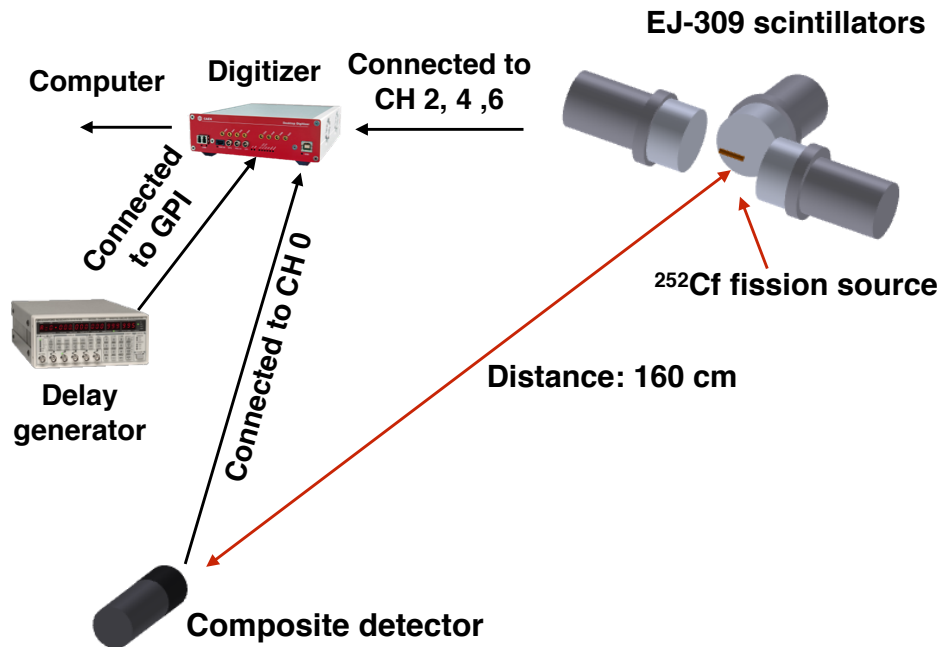
**Figure 3.1.** Experimental setup for the TOF measurement. Three EJ-309 liquid scintillators were used to tag the fission events. The composite detector was placed 160 cm away from the $^{252}$Cf fission source. The delay generator was connected to the digitizer to serve as an external trigger. All the detectors were connected to the high voltage power supply and the digitizer, which were both controlled by the CAEN standard firmware from the computer.

place in the EJ-290 scintillator, were used to select the thermalization events that precede the neutron thermalization pulses.

The digitizer used for data discretization (CAEN DT5730) has a sampling rate of 500 MHz, which corresponds to 2 ns/sample. The time delay between different digitizer channels was determined and corrected for by placing all detectors at equal distances from a pure gamma source. The data acquisition system (DAQ), including the photomultiplier rise time, had an overall time resolution of 4.8 ns, measured at full-width-half-maximum of the inter-pulse delay distribution, as represented in Fig. 3.2. The peak centered at ∼5 ns is attributed to the prompt gamma arrival time difference between the two detectors due to the different distances of travel of two gamma rays. The peak centered at ∼ 70 ns is attributed to the difference in arrival time of a neutron in the composite detector and the gamma event in the
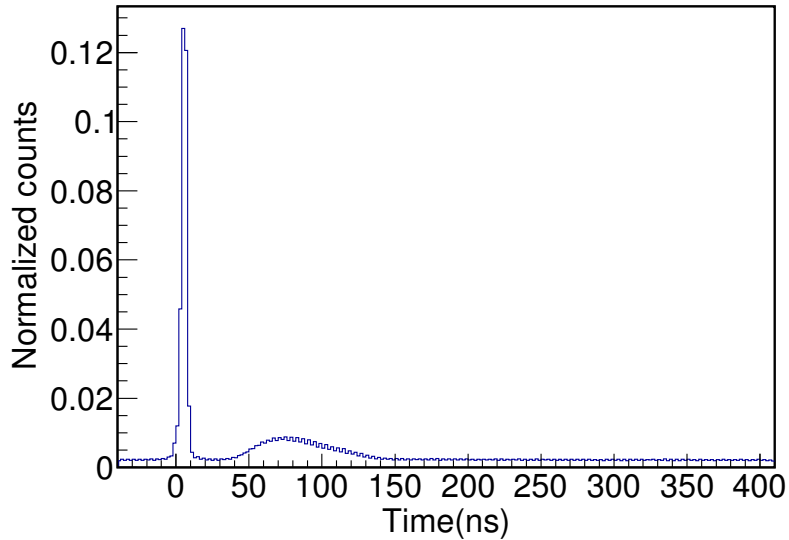
**Figure 3.2.** Normalized distribution of the inter-pulse time difference between the composite detector and the EJ-309 liquid scintillation detector after the time delay correction in the TOF measurement with the use of $^{252}$Cf source.

EJ-309 detector. The composite detector was calibrated by the Compton edge of the $^{137}$Cs source (0.477 MeV) and $^{60}$Co source (0.963 MeV). The finite voltage gain shift over time was also taken into account since the data were collected over multiple days. The DAQ was triggered by events occurring in the composite detector, using a pretrigger record length of ∼550 ns to identify an immediately preceding fission event. A delay generator (SRS DG645) was connected to the digitizer and served as an external trigger to record the time difference between the thermalization and the capture pulse, which were saved into two separate waveforms. A six-hour-long neutron shadow cone experiment was also performed using the method described in [21] and [41] to account for the contribution of the neutron room scatter. The shadow cone measurements determined that ∼ 3% of all events that were selected by the described criteria arise from neutron arriving indirectly, *i.e.* through room scatter. The waveform data were collected using the ADAQ data acquisition toolkit developed by Hartwig *et al.* [42]. The post-analysis of the data was performed based on ROOT data analysis framework [43]. Since the ADAQ software was also built using the ROOT framework, rapid data format conversion and analysis was possible.

## 3.2 Results and Discussions

The data were analyzed using the capture-gated coincidence technique. If the pulse prior to neutron capture is not identified as another neutron capture, it is considered to be a thermalization pulse. There is a possibility for uncorrelated events to be recorded in this fashion. However, the rate of uncorrelated events is relatively low, as discussed later in this section. Fig. 3.3 shows the PSP plot of the capture events and the thermalization events from the TOF measurement, which were all correlated to the incident neutron energy. The thermalization events were positioned at the same region as the gamma events due to the fact that the EJ-290 scintillator by itself does not exhibit PSD capability.

The thermalization pulse light output was calibrated to electron equivalent energy using the total pulse area. As can be seen in Fig. 3.4, the thermalization light output at any incident neutron energy shows a sharp maximum and clustering into a band. This is expected because the neutron capture cross section of $^6$Li decreases rapidly with neutron energy, so that neutrons deposit nearly all of their energy prior to capture. Even though the energy deposition does not necessarily result in the same light output due to a variety of possible scattering sequences on hydrogen and carbon and the differences in quenching, in most of the events the light output reflects a nearly complete energy deposition of the incident neutron in the EJ-290 scintillator. The characteristic range of light output results in a finite width of the light output band, which is readily discerned in Fig. 3.4. The maximum of the light output at any given neutron energy, observed as the sharp band cutoff, is attributed to a single neutron backscatter on hydrogen, in which the entire neutron energy is deposited in a single collision. At higher neutron energies, inelastic scattering and competing reactions such as $^{12}$C(n,$\alpha$)$^9$Be, $^{12}$C(n,n')3$\alpha$ with a threshold of 6.17 MeV and 7.98 MeV, respectively, could also complicate the detector response [44]. The correlated thermalization-to-capture time extracted from the TOF measurement shows good agreement with Monte Carlo simulation corrected for the expected exponentially decaying accidental coincidence rate, as shown in Fig. 3.5. The obtained capture time distribution also confirms the choice of the gating time in the experiment.

The thermalization pulse area spectra have been extracted in the range of 0.3 MeV–2.3 MeV with a bin size of 200 keV and are shown in Fig. 3.6. In the

(a)



(b)
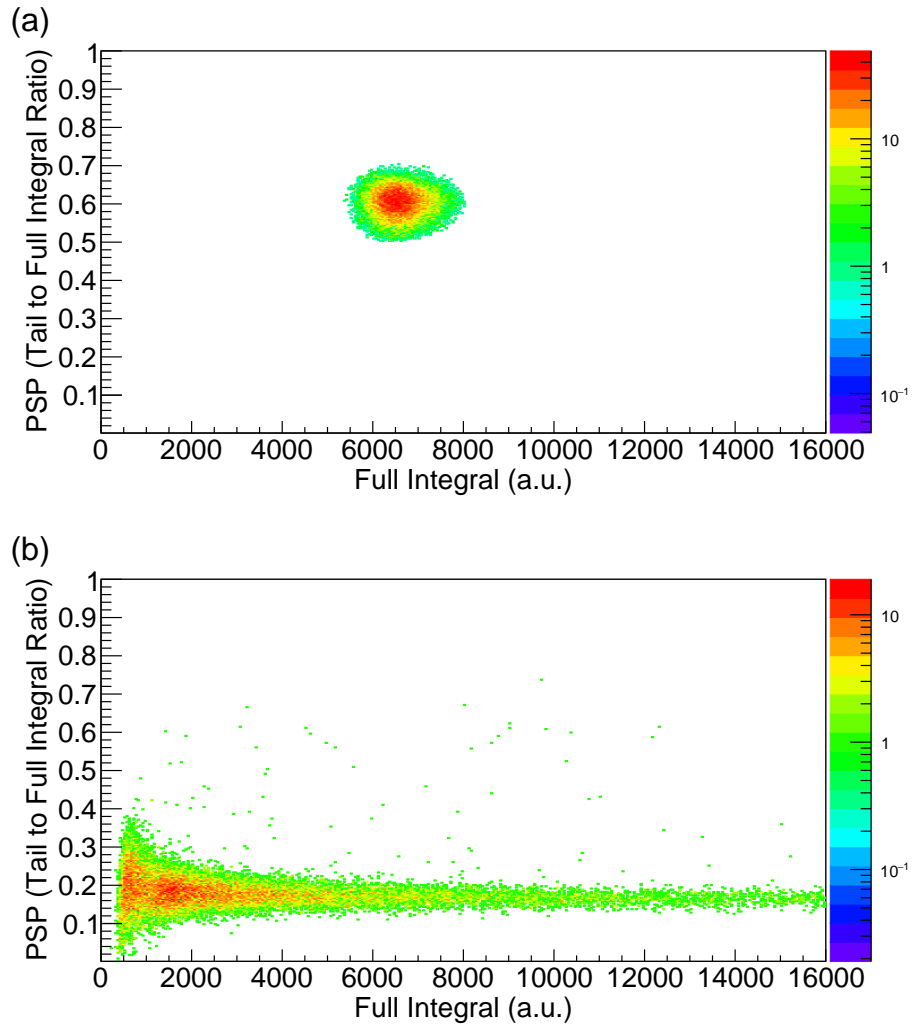


**Figure 3.3.** Relationship between PSP and total pulse integral for (a) capture events and (b) thermalization events from the TOF measurement.

range of 0.3–1.1 MeV, the shape of the spectrum resembles a single peak. As the energy is increased, the peak is broadened and it cannot be resolved equally well due in part to the low efficiency of the compact detector at higher neutron energy. Such peak broadening has also been witnessed in a previous measurement that used a monoenergetic DD neutron source (2.45 MeV) [38]. As discussed earlier, this feature of the spectrum is a consequence of the variation of the scattering sequence prior to neutron capture. Nevertheless, the continuum extending to low light output is largely suppressed and a peak-like structure can be observed, unlike the spectra measured in non-capture-gated organic scintillators in the same energy
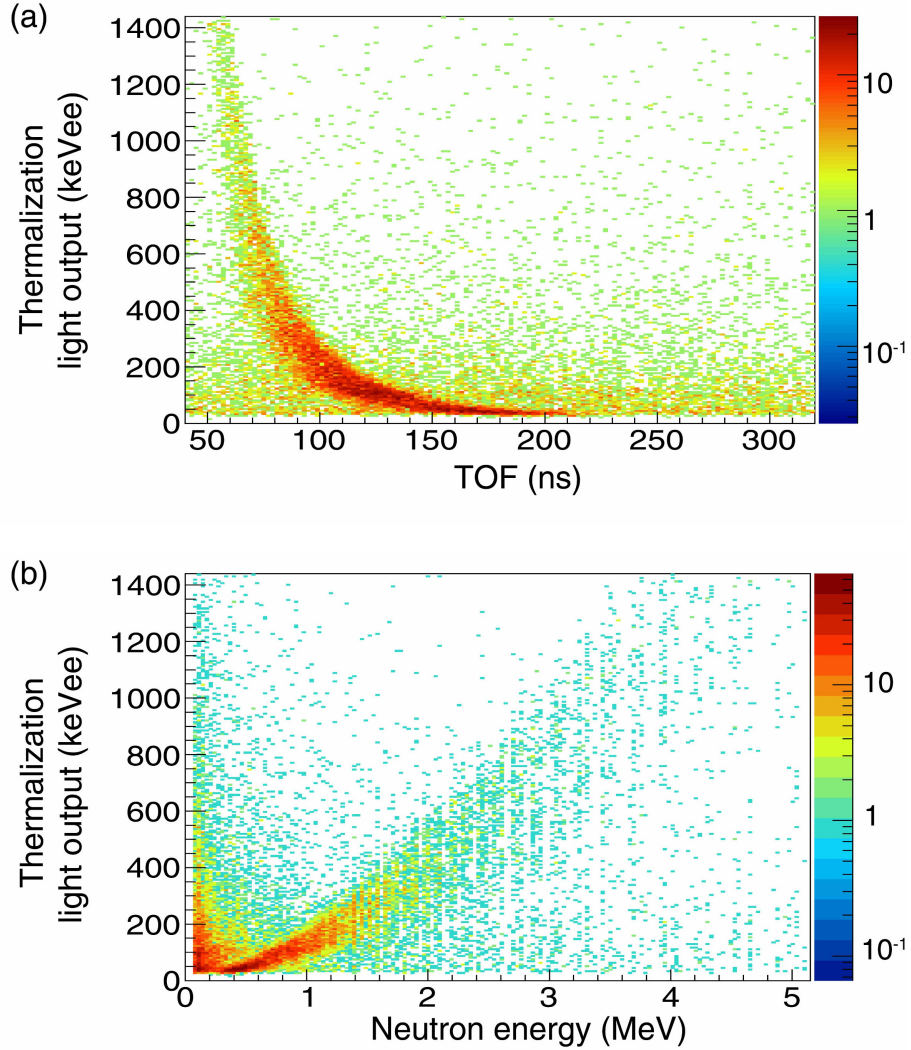
**Figure 3.4.** Relationship between (a) thermalization light output and TOF and (b) thermalization light output and neutron energy calculated from the TOF. The thermalization light output forms a band showing a clear nonproportional correlation with neutron energy. Events are largely concentrated at neutron energies ⩽2 MeV due to a combination of the shape of the neutron fission spectrum of $^{252}$Cf and the reduction of detector efficiency with increasing neutron energy. At low neutron energies (⩽0.2 MeV), the room scatter and accidental events become significant.

region [45]. The maximum light output corresponds to a complete energy transfer of a neutron in a single collision with a hydrogen nucleus because of the concave nonproportionality of the PVT-based scintillator [46]. Multiple collisions with hydrogen and carbon atoms generate less light output due to the nonproportional
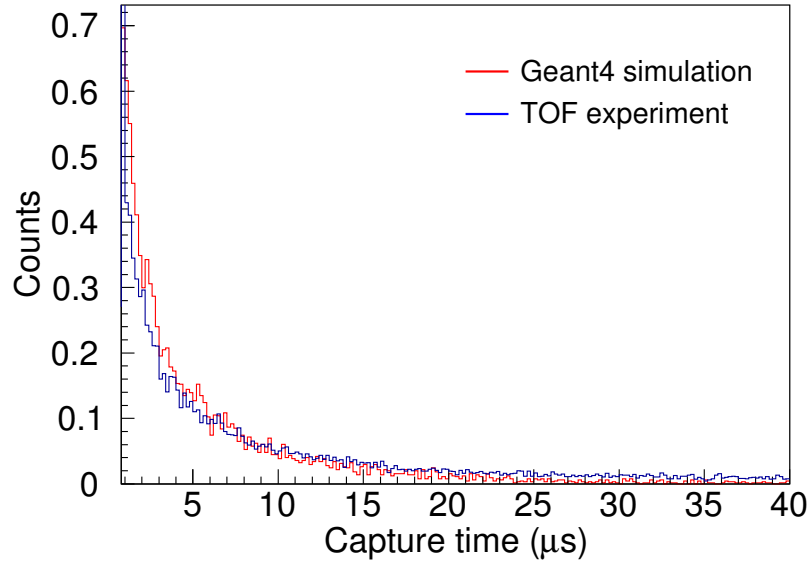
**Figure 3.5.** Measured and simulated thermalization-to-capture time with $^{252}$Cf source normalized to the number of events detected from 0.8 µs to 40 µs. The measured events are all correlated with the TOF of the incident neutron. The shortest measured capture time of 0.8 µs is limited by the waveform record length.
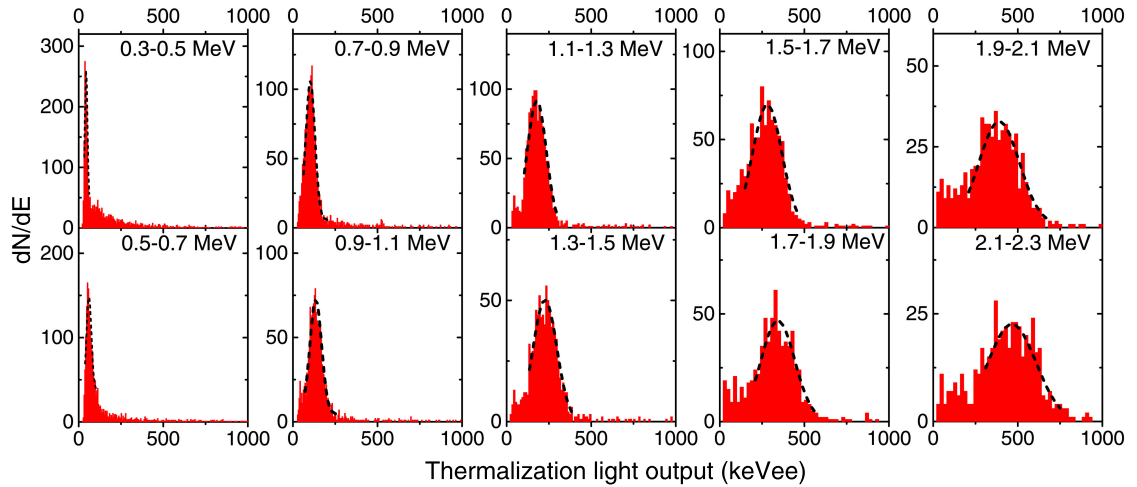


**Figure 3.6.** Thermalization pulse area spectra with a neutron energy bin size of 200 keV. The thermalization light output is calibrated to the electron equivalent energy, where bin widths of 5 keVee, 10 keVee, and 20 keVee were applied for the 0.3–1.1 MeV, 1.1–1.5 MeV, and 1.5–2.3 MeV region, respectively to account for statistical limitations at higher neutron energies. The black dashed curve represents a Gaussian fit to the high energy part of the spectrum.

quenching factor of the nuclear recoils [47, 48]. Furthermore, based on Geant4 simulation, a fraction of the neutrons are captured before their kinetic energy is fully dissipated in collisions, which can also account for a fraction of the peak broadening.

The ideal spectral feature generated is further broadened by the intrinsic resolution of the detector electronics and the neutron energy resolution from the TOF measurement. To determine the nonlinear response of the detector, the falling edges of the spectra in Fig. 3.6 have been fitted by a sum of a Gaussian and a constant to account for accidentals: $f(x) = a \exp\left[-(x-b)^2/(2c^2)\right] + d$. At low neutron energies (0.3–0.7 MeV), the low-energy side of the peak is broadened by accidentals such as room scatters. Therefore, a constant was used to account for those accidental events. However, at higher neutron energies, the constant $d$ is close to zero. The peak location of the Gaussian fit is attributed to the light output generated by a single scatter on hydrogen, where neutron transfers its entire kinetic energy to a single proton. Combined with the previously conducted measurements with monoenergetic neutron sources (DD, 2.45 MeV and DT, 14.1 MeV) [38], Fig. 3.7 shows the fit to Birks [25] and Chou [49] descriptions of energy-dependent light output. The Birks semi-empirical formula,

$$L(E) = \int_0^E \frac{dL}{dx} dx = L_0 \int_0^E \frac{dE}{1 + kb\, dE/dx}, \tag{3.2}$$

has been successfully applied in explaining the experimental recoil nonproportionality in organic scintillators at both low energy ($<1$ MeV) [50] and high energy up to 20 AMeV (AMeV being a unit that describes energy-per-nucleon) [51]. Here, $E$ is the initial particle energy, $L$ is the total light output, $-dE/dx$ is the stopping power, and $L_0$ and $kb$ are the fit parameters. According to Birks' theory, "damaged" molecules are produced locally along the track of the charged recoil and serve as the quenching agents for non-radiative recombination [25]. The term $kb\,(dE/dx)$ is a measure of the damaged molecule concentration that accounts for the energy-dependent quenching nonproportionality.

Chou proposed an alternative description that includes one additional parameter, $C$, to account for different modes of excitations [49]:

$$L(E) = \int_0^E \frac{dL}{dx} dx = L_0 \int_0^E \frac{dE}{1 + kb\, dE/dx + C\,(dE/dx)^2}. \tag{3.3}$$

For both fitting formulas, the stopping power data of the PVT-based scintillator from the NIST pstar library were used. [52]

(a)
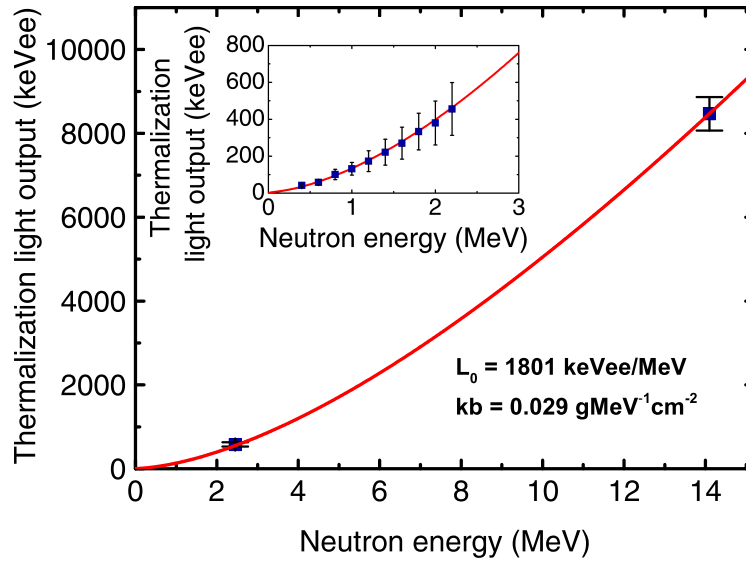


(b)
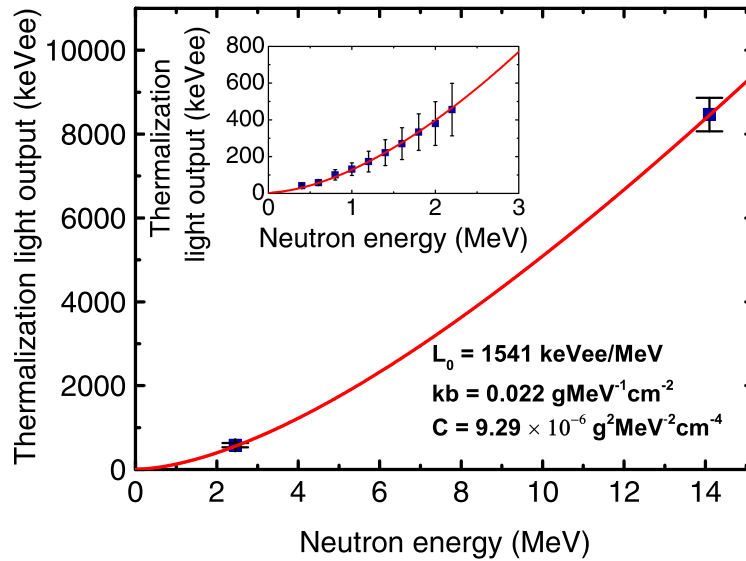


**Figure 3.7.** (a) Birks formula fit and (b) Chou formula fit with TOF and monoenergetic neutron data. The monoenergetic data points are shown in the full-size image, while TOF data points are shown in the inset. The fit parameters are displayed in the figure.

(a)
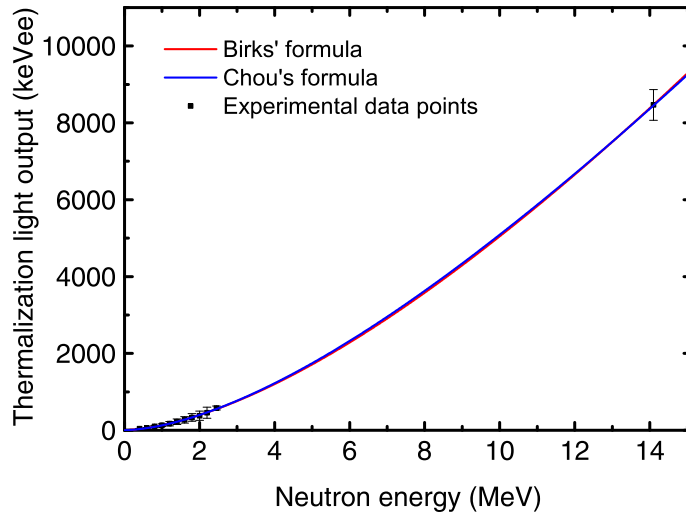


(b)
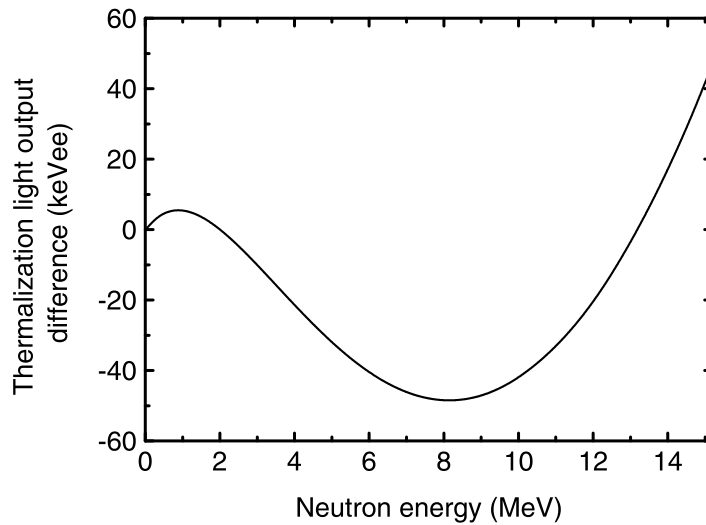
**Figure 3.8.** (a) Comparison between the Birks' fit and the Chou's fit (b) Thermalization light output difference between the Birks' fit and the Chou's fit.

As shown in Fig. 3.7, both the Birks' and the Chou's approach describe the trend in light output seen in TOF and monoenergetic neutron measurements. The difference between the Birks' fit and the Chou's fit is relatively small, as shown in Fig. 3.8. The Birks formula, which is also more widely used, seems sufficient to describe the nonproportionality of the EJ-290 polymer. EJ-290 PVT-based polymer and its equivalents have not been previously characterized in this manner. However,

if compared with other PVT-based plastic scintillators, similar fit parameters $kb$ and $C$ are found [46]. We note that the material composition and the fabrication process (homogeneous mixture of resin, solvent and catalyst, degassing process, etc.) all have a significant influence on the detector response. The obtained nonlinear fitting curve can further be used to correlate the neutron energy from the thermalization pulse area spectrum for spectroscopic analysis.

# Chapter 4
# Geant4 Simulation of Detector Response

Geant4 simulation of the detector geometry was developed by Mayer *et al.* [35]. The neutron collision sequence, which cannot be obtained experimentally using the experimental setup employed, can be extracted from the Geant4 simulation and used to help understand the detector response as well as the results obtained from the TOF measurement. The real detector geometry is defined in Geant4, as shown in Fig. 4.1. The gray cylinder represents the PVT material, while the blue rods represent the lithium-doped GS20 glass.
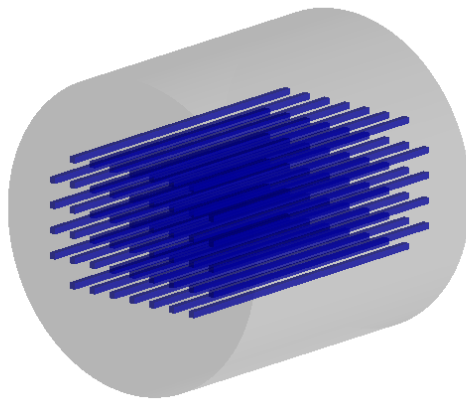


**Figure 4.1.** Composite detector geometry defined in Geant4 (image courtesy of Nattress *et al.*).

A variety of information including the particle type, particle energy, energy loss during the collision, inter-collision time as well as the process name can be retrieved from Geant4 simulation. An example of the output collision information is illustrated in Appendix A. The post-analysis code for the results shown in this chapter is presented in Appendix B.
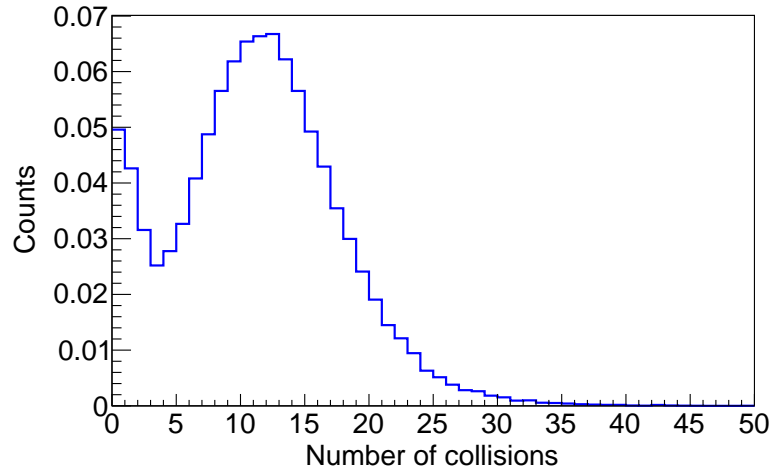
**Figure 4.2.** Geant4 simulation showing the normalized number of collisions with hydrogen and carbon nuclei for detector irradiated by a $^{252}$Cf fission source, when neutron capture is required. A total of 62948 scattered neutrons is shown and is normalized to a single scatter.
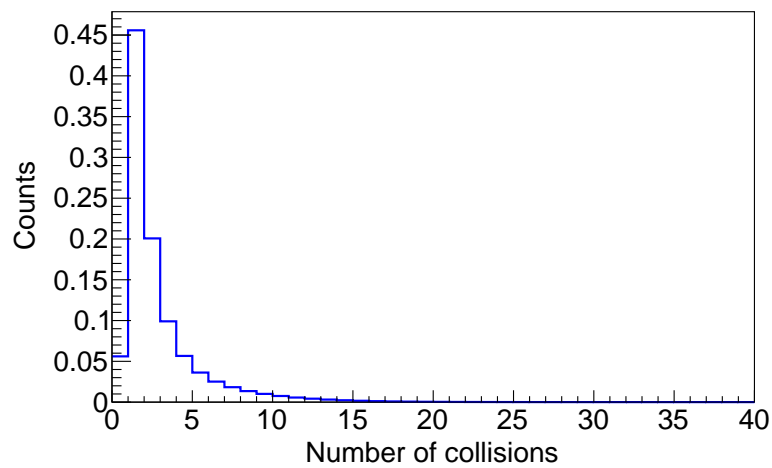


**Figure 4.3.** Geant4 simulation showing the normalized number of collisions with hydrogen and carbon nuclei for detector irradiated by a $^{252}$Cf fission source, when neutron capture is not required. A total of 4102666 scattered neutrons is shown and is normalized to a single scatter.

With an incident $^{252}$Cf neutron fission spectrum, the number of collisions with hydrogen and carbon nuclei within the PVT before the neutron capture was determined from Geant4 simulation and is shown in Fig. 4.2. There are on average 10.8 collisions with hydrogen and carbon nuclei prior to neutron capture. In comparison, as shown in Fig. 4.3, the average number of neutron collisions not gated by neutron capture is 4.3, which is much lower than that when neutron capture is required. When neutron capture is required, on average more energy is transferred to the scintillator. Therefore, the thermalization pulse has a stronger correlation with the incident neutron energy in comparison to the conventional proton recoil detector. Among all the captured events, approximately 3.2% of the neutrons undergo only one collision with hydrogen prior to capture, while 1.0% undergo only one collision with carbon.
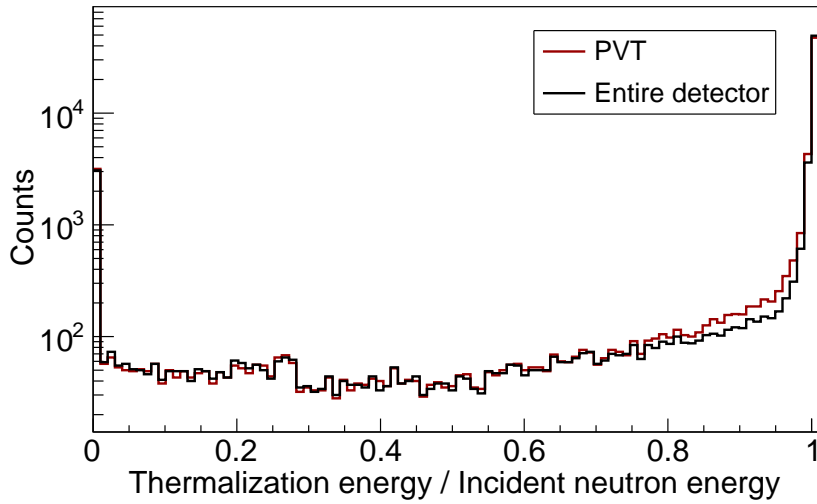


**Figure 4.4.** Geant4 simulation of the ratio of the neutron energy deposition at the time of capture to its incident energy in the PVT (red curve) and in the entire detector (black curve) for neutrons incident from a $^{252}$Cf source.

The ratio of a neutron energy loss at the time of capture to its incident energy within PVT and the total detector volume is shown in Fig. 4.4. It can be seen that the captured neutrons tend to deposit most of their energy prior to capture. The energy loss in PVT is more significant than that in the $^6$Li-doped glass due to its larger volume and superior moderation capability. About 75% of the neutrons lose more than 99% of their energy at the time of capture by proton or carbon recoil
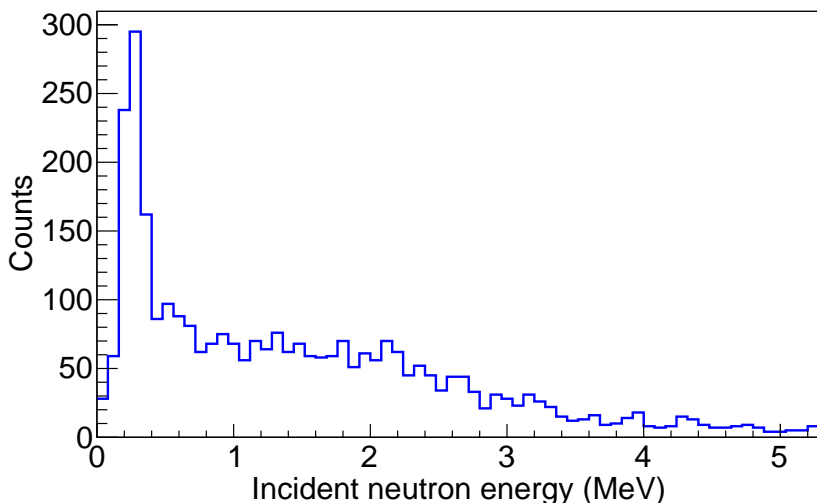
**Figure 4.5.** Geant4 simulation of the incident neutron energy spectrum for neutrons that are captured directly without any scattering interaction within PVT.

(most of the counts are located in the last few bins in Fig. 4.4). Approximately 40% of the neutrons are captured after they are fully thermalized, with energy below 0.025 eV. It is noteworthy that even though the term "thermalization pulse" is used, not all the captured neutrons are fully thermalized at the time of capture; some remain in the epithermal neutron region or at even higher energies.

As can be observed in the first bin of the Fig. 4.4, approximately 5% of the neutrons are captured without any scattering event taking place within either PVT or glass rods, meaning that no energy loss occurred for these neutrons at the time of capture. The incident neutron energy of these events, which is the same as the energy at the time of capture, is shown in Fig. 4.5. This feature of neutron capture without scattering can be explained by the $^6$Li neutron capture cross section resonance centered at 240 keV, as shown in Fig. 1.1. The peak in Fig. 4.5 is also centered at 240 keV, signifying the preference for neutron capture on $^6$Li near this resonance region, where the neutrons are not fully moderated.

In Fig. 4.6 (a), we can visualize the event distribution of the number of scatters with hydrogen and carbon nuclei before the neutron capture. There are on average more collisions with hydrogen (or proton) than carbon. Even though the energy transfer to carbon is on average lower than that to hydrogen because of its higher atomic mass, the light yield from carbon collisions may not be negligible for the

35
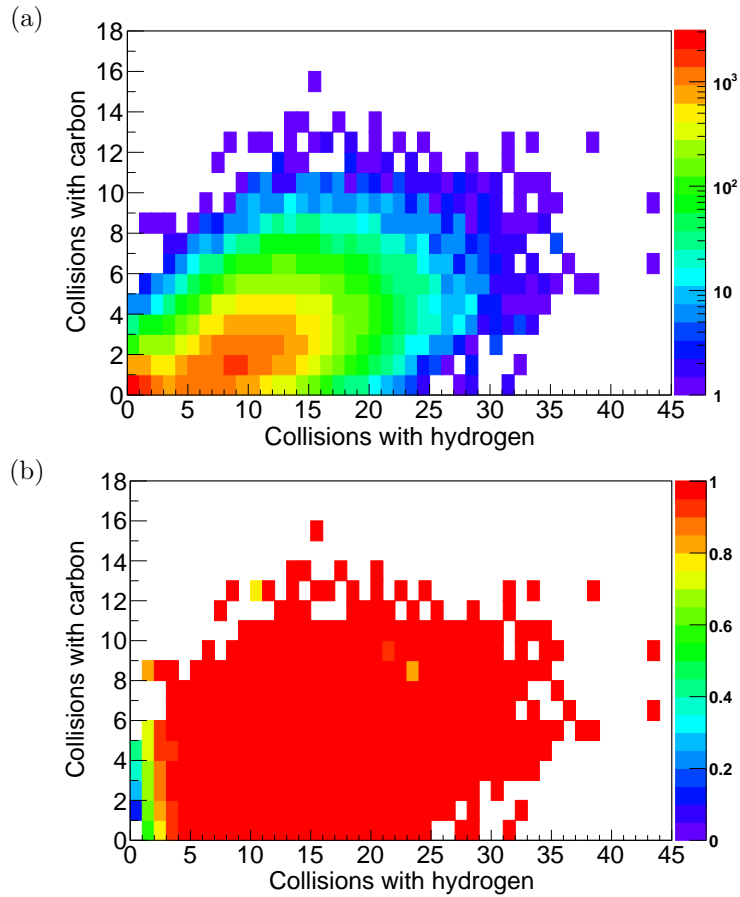
**Figure 4.6.** 2D histogram of (a) the number of neutron capture events and (b) the average ratio of neutron energy deposition to incident neutron energy, as a function of the number of collisions with hydrogen and carbon nuclei at the time of capture irradiated with $^{252}$Cf neutron source. A total of 62948 events is shown. The periphery white area signifies no capture event for the corresponding bin.

capture gated event, as a significant number of carbon scatters takes place, as shown in Fig. 4.6. From Fig. 4.6 (b), we can observe that the average energy deposition ratio is very close to unity for capture events that have more than two collisions with hydrogen, and low energy deposition in general corresponds to lower number of scatters on either carbon or hydrogen. This result could help optimize the detector geometry or composition in order to maximize the neutron energy deposition. If the light output simulation of the light yield nonproportionality with different charged particles (proton, carbon, etc.) can also be successfully modeled, the combination of these simulation results would be helpful for future detector design.

# Chapter 5
# Summary and Conclusions

In this work, the composite detector was characterized through capture-gated coincidence technique. The nonproportional dependence of the scintillation light yield in the PVT material EJ-290 as a function of neutron energy deposition has been characterized by TOF measurement. For a given incident neutron energy, the thermalization light output spectrum exhibits a more peak-like shape compared to scintillation detector that does not employ capture gating. This is because of the preference for nearly complete energy deposition prior to neutron capture. A broadened peak is observed and is attributed to the multiple scattering sequence, the energy-dependent quenching for hydrogen and carbon recoils, as well as the intrinsic resolution of the DAQ. Combined with previous measurements using monoenergetic neutron sources at 2.45 MeV and 14.1 MeV, the light output nonproportionality of the EJ-290 PVT resulting from energy-dependent quenching is described via the Birks and Chou parametrizations, both of which produce good fits to experimental results. From the Geant4 simulation of the composite detector, the neutron collision histories have been analyzed. These simulation results provide a better understanding of the neutron interaction physics inside the detector and may be used for future detector design optimization.

In the future, Geant4 simulations should provide a more in-depth analysis of the collision sequence histories with monoenergetic neutrons over a range of energies. In addition, it would be very interesting to implement the light output module and the optical photon transport module in Geant4. However, due to the large number of optical photons generated per interaction and the complex geometry of the composite detector, a substantial computational capability may be required. If the optical photon module can be successfully implemented and benchmarked, a direct comparison between the experimental results and simulation results can be achieved,

which will help understand the features seen in the measured thermalization light output spectra.

Regarding future experiments, spectroscopic characterization of the composite detector with extended neutron or proton energy range would be beneficial. If the detector response and the detector efficiency for different neutron energies can be obtained successfully either from the experiment or from the simulation, spectrum reconstruction with neutron unfolding can also be performed. It would also be interesting to compare the neutron unfolding results between the use of response matrix and the event-by-event reconstruction scheme.

# Bibliography

[1] J. A. Formaggio and C. J. Martoff, "Backgrounds to sensitive experiments underground," *Annu. Rev. Nucl. Part. Sci.*, vol. 54, pp. 361–412, 2004.

[2] S. R. Elliott and J. Engel, "Double-beta decay," *J. Phys. G. Nucl. Part. Phys*, vol. 30, no. 9, p. R183, 2004.

[3] X. Yan, U. Titt, A. Koehler, and W. Newhauser, "Measurement of neutron dose equivalent to proton therapy patients outside of the proton radiation field," *Nucl. Instrum. Methods Phys. Res., Sect. A*, vol. 476, no. 1, pp. 429–434, 2002.

[4] J. B. Czirr, D. B. Merrill, D. Buehler, T. K. McKnight, J. L. Carroll, T. Abbott, and E. Wilcox, "Capture-gated neutron spectrometry," *Nucl. Instrum. Methods Phys. Res., Sect. A*, vol. 476, no. 1, pp. 309–312, 2002.

[5] M. Flaska and S. A. Pozzi, "Identification of shielded neutron sources with the liquid scintillator BC-501A using a digital pulse shape discrimination method," *Nucl. Instrum. Methods Phys. Res., Sect. A*, vol. 577, no. 3, pp. 654–663, 2007.

[6] K. Gamage, M. Joyce, and N. Hawkes, "A comparison of four different digital algorithms for pulse-shape discrimination in fast scintillators," *Nucl. Instrum. Methods Phys. Res., Sect. A*, vol. 642, no. 1, pp. 78–83, 2011.

[7] A. Poitrasson-Rivière, M. C. Hamel, J. K. Polack, M. Flaska, S. D. Clarke, and S. A. Pozzi, "Dual-particle imaging system based on simultaneous detection of photon and neutron collision events," *Nucl. Instrum. Methods Phys. Res., Sect. A*, vol. 760, pp. 40–45, 2014.

[8] T. Zak, S. D. Clarke, M. M. Bourne, S. A. Pozzi, Y. Xu, T. J. Downar, and P. Peerani, "Neutron spectroscopy of plutonium oxide using matrix unfolding approach," *Nucl. Instrum. Methods Phys. Res., Sect. A*, vol. 622, no. 1, pp. 191–195, 2010.

[9] A. Simpson, S. Jones, M. Clapham, and S. McElhaney, "A review of neutron detection technology alternatives to helium-3 for safeguards applications," in *INMM 52nd Annual Meeting*, vol. 8, 2011.

[10] R. T. Kouzes, A. T. Lintereur, and E. R. Siciliano, "Progress in alternative neutron detection to address the helium-3 shortage," *Nucl. Instrum. Methods Phys. Res., Sect. A*, vol. 784, pp. 172–175, 2015.

[11] G. F. Knoll, *Radiation detection and measurement.* John Wiley & Sons, pp. 521–522, 2010.

[12] W. R. Mills Jr, R. L. Caldwell, and I. L. Morgan, "Low voltage $^3$He-filled proportional counter for efficient detection of thermal and epithermal neutrons," *Rev. Sci. Instrum.*, vol. 33, no. 8, pp. 866–868, 1962.

[13] P. Dighe, D. Prasad, K. Prasad, S. Kataria, S. Athavale, A. Pappachan, and A. Grover, "Boron-lined proportional counters with improved neutron sensitivity," *Nucl. Instrum. Methods Phys. Res., Sect. A*, vol. 496, no. 1, pp. 154–161, 2003.

[14] C. Bass, E. Beise, H. Breuer, C. Heimbach, T. Langford, and J. Nico, "Characterization of a $^6$Li-loaded liquid organic scintillator for fast neutron spectrometry and thermal neutron detection," *Appl. Radiat. Isotopes*, vol. 77, pp. 130–138, 2013.

[15] V. Mares, G. Schraube, and H. Schraube, "Calculated neutron response of a bonner sphere spectrometer with $^3$He counter," *Nucl. Instrum. Methods Phys. Res., Sect. A*, vol. 307, no. 2, pp. 398–412, 1991.

[16] H. Toyokawa, A. Uritani, C. Mori, N. Takeda, and K. Kudo, "A spherical neutron counter with an extended energy response for dosimetry," *Radiat. Prot. Dosim.*, vol. 70, no. 1-4, pp. 365–370, 1997.

[17] A. Santamarina, D. Bernard, P. Blaise, M. Coste, A. Courcelle, T. Huynh, C. Jouanne, P. Leconte, O. Litaize, S. Mengelle, *et al.*, "The jeff-3.1. 1 nuclear data library," *JEFF report*, vol. 22, no. 10.2, p. 2, 2009.

[18] V. Verbinski, W. Burrus, T. Love, W. Zobel, N. Hill, and R. Textor, "Calibration of an organic scintillator for neutron spectrometry," *Nucl. Instrum. Methods*, vol. 65, no. 1, pp. 8–25, 1968.

[19] H. Werle, "Neutron spectrometry with proton-recoil proportional counters in the energy region up to 10 MeV," *Nucl. Instrum. Methods*, vol. 99, no. 2, pp. 295–300, 1972.

[20] J. B. Czirr and G. L. Jensen, "A compact neutron coincidence spectrometer, its measured response functions and potential applications," *Nucl. Instrum. Methods Phys. Res., Sect. A*, vol. 349, no. 2, pp. 532–539, 1994.

[21] M. Mayer, J. Nattress, V. Kukharev, A. Foster, A. Meddeb, C. Trivelpiece, Z. Ounaies, and I. Jovanovic, "Development and characterization of a neutron detector based on a lithium glass–polymer composite," *Nucl. Instrum. Methods Phys. Res., Sect. A*, vol. 785, pp. 117–122, 2015.

[22] B. Fisher, J. Abdurashitov, K. Coakley, V. Gavrin, D. Gilliam, J. Nico, A. Shikhin, A. Thompson, D. Vecchia, and V. Yants, "Fast neutron detection with $^6$Li-loaded liquid scintillator," *Nucl. Instrum. Methods Phys. Res., Sect. A*, vol. 646, no. 1, pp. 126–134, 2011.

[23] S. Jastaniah and P. Sellin, "Digital techniques for n/$\gamma$ pulse shape discrimination and capture-gated neutron spectroscopy using liquid scintillators," *Nucl. Instrum. Methods Phys. Res., Sect. A*, vol. 517, no. 1, pp. 202–210, 2004.

[24] G. F. Knoll, *Radiation detection and measurement.* John Wiley & Sons, pp.586–589, 2010.

[25] J. B. Birks, "Scintillations from organic crystals: specific fluorescence and relative response to different radiations," *Proc. Phys. Soc. London Sect. A*, vol. 64, no. 10, p. 874, 1951.

[26] R. Craun and D. Smith, "Analysis of response data for several organic scintillators," *Nucl. Instrum. Methods*, vol. 80, no. 2, pp. 239–244, 1970.

[27] P. Holm, K. Peräjärvi, S. Ristkari, T. Siiskonen, and H. Toivonen, "A capture-gated neutron spectrometer for characterization of neutron sources and their shields," *Nucl. Instrum. Methods Phys. Res., Sect. A*, vol. 751, pp. 48–54, 2014.

[28] W. Feldman, G. Auchampaugh, and R. Byrd, "A novel fast-neutron detector for space applications," *Nucl. Instrum. Methods Phys. Res., Sect. A*, vol. 306, no. 1, pp. 350–365, 1991.

[29] E. Kamykowski, "Comparison of calculated and measured spectral response and intrinsic efficiency for a boron-loaded plastic neutron detector," *Nucl. Instrum. Methods Phys. Res., Sect. A*, vol. 317, no. 3, pp. 559–566, 1992.

[30] T. Aoyama, K. Honda, C. Mori, K. Kudo, and N. Takeda, "Energy response of a full-energy-absorption neutron spectrometer using boron-loaded liquid scintillator BC-523," *Nucl. Instrum. Methods Phys. Res., Sect. A*, vol. 333, no. 2-3, pp. 492–501, 1993.

[31] M. Flaska, S. Pozzi, B. Czirr, *et al.*, "Use of an LGB detector in nuclear nonproliferation applications," in *Proc. IEEE Nucl. Sci. Symp. Conf. Rec.*, pp. 3376–3380, IEEE, 2008.

[32] J. Abdurashitov, V. Gavrin, A. Kalikhov, V. Matushko, A. Shikhin, V. Yants, O. Zaborskaia, J. Adams, J. Nico, and A. Thompson, "A high resolution, low background fast neutron spectrometer," *Nucl. Instrum. Methods Phys. Res., Sect. A*, vol. 476, no. 1, pp. 318–321, 2002.

[33] S. A. Pozzi, R. Oberer, and J. S. Neal, "Analysis of the response of capture-gated organic scintillators," *IEEE Trans. Nucl. Sci*, vol. 52, no. 6, pp. 3141–3146, 2005.

[34] S. A. Pozzi, J. A. Mullens, and J. T. Mihalczo, "Analysis of neutron and photon detection position for the calibration of plastic (BC–420) and liquid (BC–501) scintillators," *Nucl. Instrum. Methods Phys. Res., Sect. A*, vol. 524, no. 1, pp. 92–101, 2004.

[35] M. Mayer, J. Nattress, C. Trivelpiece, and I. Jovanovic, "Geometric optimization of a neutron detector based on a lithium glass–polymer composite," *Nucl. Instrum. Methods Phys. Res., Sect. A*, vol. 784, pp. 168–171, 2015.

[36] E. TECHNOLOGY, "Table of physical constants of scintillators," 2011.

[37] S.-G. Crystals, "Lithium glass scintillators," 2015.

[38] J. Nattress, M. Mayer, A. Foster, A. Meddeb, C. Trivelpiece, Z. Ounaies, and I. Jovanovic, "Capture-gated spectroscopic measurements of monoenergetic neutrons with a composite scintillation detector," *IEEE Trans. Nucl. Sci*, vol. 63, pp. 1–0, 2016.

[39] C.-K. C. Wang, *Progress in californium-252 neutron brachytherapy.* INTECH Open Access Publisher, 2012.

[40] S. Agostinelli, J. Allison, K. a. Amako, J. Apostolakis, H. Araujo, P. Arce, M. Asai, D. Axen, S. Banerjee, G. Barrand, *et al.*, "Geant4–a simulation toolkit," *Nucl. Instrum. Methods Phys. Res., Sect. A*, vol. 506, no. 3, pp. 250–303, 2003.

[41] C. Eisenhauer, J. Hunt, and R. Schwartz, "Calibration techniques for neutron personal dosimetry," *Radiat. Prot. Dosim.*, vol. 10, no. 1-4, pp. 43–57, 1985.

[42] Z. S. Hartwig, "The ADAQ framework: An integrated toolkit for data acquisition and analysis with real and simulated radiation detectors," *Nucl. Instrum. Methods Phys. Res., Sect. A*, 2016.

[43] R. Brun and F. Rademakers, "ROOT–an object oriented data analysis framework," *Nucl. Instrum. Methods Phys. Res., Sect. A*, vol. 389, no. 1, pp. 81–86, 1997.

[44] G. F. Knoll, *Radiation detection and measurement.* John Wiley & Sons, pp.579, 2010.

[45] N. Kornilov, I. Fabry, S. Oberstedt, and F.-J. Hambsch, "Total characterization of neutron detectors with a $^{252}$Cf source and a new light output determination," *Nucl. Instrum. Methods Phys. Res., Sect. A*, vol. 599, no. 2, pp. 226–233, 2009.

[46] L. Torrisi, "Plastic scintillator investigations for relative dosimetry in proton-therapy," *Nucl. Instrum. Methods Phys. Res., Sect. B*, vol. 170, no. 3, pp. 523–530, 2000.

[47] A. Enqvist and I. Pázsit, "Calculation of the light pulse distributions induced by fast neutrons in organic scintillation detectors," *Nucl. Instrum. Methods Phys. Res., Sect. A*, vol. 618, no. 1, pp. 266–274, 2010.

[48] A. Enqvist, C. C. Lawrence, B. M. Wieger, S. A. Pozzi, and T. N. Massey, "Neutron light output response and resolution functions in EJ-309 liquid scintillation detectors," *Nucl. Instrum. Methods Phys. Res., Sect. A*, vol. 715, pp. 79–86, 2013.

[49] C. Chou, "The nature of the saturation effect of fluorescent scintillators," *Phys. Rev.*, vol. 87, no. 5, p. 904, 1952.

[50] L. Reichhart, D. Y. Akimov, H. Araújo, E. Barnes, V. Belov, A. Burenkov, V. Chepel, A. Currie, L. DeViveiros, B. Edwards, *et al.*, "Quenching factor for low-energy nuclear recoils in a plastic scintillator," *Phys. Rev. C*, vol. 85, no. 6, p. 065801, 2012.

[51] S. Nyibule, J. Tõke, E. Henry, W. Schröder, L. Acosta, L. Auditore, G. Cardella, E. De Filippo, L. Francalanza, S. Gianì, *et al.*, "Birks' scaling of the particle light output functions for the EJ 299-33 plastic scintillator," *Nucl. Instrum. Methods Phys. Res., Sect. A*, vol. 768, pp. 141–145, 2014.

[52] M. Berger, J. Coursey, M. Zucker, and J. Chang, "Stopping-power and range tables for electrons, protons, and helium ions (2005)," *Available on http://physics. nist. gov*, 2015.

# Appendix A
# Collision History Information from Geant4 Simulation

Example of collision history information extracted from Geant4 simulation is presented this section. The particle collision history can be obtained from Geant4 simulation, as shown in Fig. A.1.

| Event ID | Step ID | Track ID | Parent ID | Particle Type | Time (μs) | Kinetic energy (keV) | Energy loss (keV) | Volume Name |
|---|---|---|---|---|---|---|---|---|
| 0 | 1 | 1 | 0 | neutron | 0 | 2873.3 | 0 | worldPhysical |
| 1 | 1 | 1 | 0 | neutron | 0 | 1122.76 | 0 | worldPhysical |
| 1 | 2 | 1 | 0 | neutron | 0.016357 | 1122.76 | 0 | PVT_Scint |
| 1 | 3 | 1 | 0 | neutron | 0.017154 | 751.992 | 0 | PVT_Scint |
| 1 | 4 | 1 | 0 | neutron | 0.017963 | 751.992 | 0 | LiG_Scint |
| 1 | 5 | 1 | 0 | neutron | 0.018065 | 751.992 | 0 | PVT_Scint |
| 1 | 6 | 1 | 0 | neutron | 0.018923 | 44.153 | 0 | PVT_Scint |
| 1 | 7 | 1 | 0 | neutron | 0.023834 | 44.153 | 0 | LiG_Scint |
| 1 | 8 | 1 | 0 | neutron | 0.024142 | 44.153 | 0 | PVT_Scint |
| 1 | 9 | 1 | 0 | neutron | 0.028258 | 44.153 | 0 | worldPhysical |
| 1 | 1 | 3 | 1 | proton | 0.018923 | 708.225 | 708.225 | PVT_Scint |
| 1 | 1 | 2 | 1 | proton | 0.017154 | 370.965 | 370.965 | PVT_Scint |
| 2 | 1 | 1 | 0 | neutron | 0 | 3259.3 | 0 | worldPhysical |
| 3 | 1 | 1 | 0 | neutron | 0 | 2679.2 | 0 | worldPhysical |
| 3 | 2 | 1 | 0 | neutron | 0.010573 | 2679.2 | 0 | PVT_Scint |
| 3 | 3 | 1 | 0 | neutron | 0.011264 | 2141.76 | 0 | PVT_Scint |
| 3 | 4 | 1 | 0 | neutron | 0.011585 | 2141.76 | 0 | LiG_Scint |
| 3 | 5 | 1 | 0 | neutron | 0.011646 | 2141.76 | 0 | PVT_Scint |
| 3 | 6 | 1 | 0 | neutron | 0.012357 | 2141.76 | 0 | worldPhysical |
| 3 | 1 | 2 | 1 | C12 | 0.011264 | 537.636 | 537.636 | PVT_Scint |

**Figure A.1.** Example of collision history information extracted from Geant4 simulation.

In Geant4, one event is defined by all the collisions generated by the same primary incident particle including the collisions of secondary particles. One step represents one collision or one particle interaction. When particles pass through volume boundaries, one step will also be created. All the collisions of the same

44

particle share one track ID. The parent ID is the parent track ID of the particle of interest. Volume name indicates the volume where the collision takes place. The volume with the name "PVT_Scint" is used to define the PVT polymer, while the name "LiG_Scint" represents the lithium-doped glass rods in the detector. The volume with the name "worldPhysical" is the envelope of all the volumes of interest. Information such as inter-collision time, kinetic energy and energy loss during the step can also be obtained from the simulation.

# Appendix B
# Geant4 Post-Analysis Code

The codes **SSNM.hh** and **SSNM.cpp** were used to analyze the collision histories of the composite detector. These analysis code have been developed by modifying an earlier version of the analysis written by Nattress *et al.*.

**SSNM.hh:**

```
#ifndef SSNM_hh
#define SSNM_hh
#include <string>
#include <TString.h>
#include <TROOT.h>
#include <TChain.h>
#include <TFile.h>
#include <iostream>
using namespace std;
TString rootfile;

class SSNM {
public :
TTree *fChain;
Int_t fCurrent;
Int_t eventID;
Int_t stepID;
Int_t trackID;
Int_t parentID;
Double_t kineticE;
Double_t pE;
Double_t x;
Double_t y;
Double_t z;
Double_t postx;
```

```
Double_t posty;
Double_t postz;
Double_t time;
string ptype;
string volumeName;
sstring pdgNum;
// List of branches TBranch *b_eventID;
TBranch *b_stepID;
TBranch *b_trackID;
TBranch *b_parentID;
TBranch *b_kineticE;
TBranch *b_pE;
TBranch *b_x;
TBranch *b_y;
TBranch *b_z;
TBranch *b_postx;
TBranch *b_posty;
TBranch *b_postz;
TBranch *b_ptype;
TBranch *b_time;
TBranch *b_volumeName;
TBranch *b_pdgNum;

SSNM(TTree *tree=0);
virtual ~SSNM();
virtual Int_t Cut(Long64_t entry);
virtual Int_t GetEntry(Long64_t entry);
virtual Long64_t LoadTree(Long64_t entry);
virtual void Init(TTree *tree);
virtual void Loop();
virtual Bool_t Notify();
virtual void Show(Long64_t entry = -1);

private:
int min_pos(int array[ ],int array_size);
double base_finder(int array[ ],int array_size);
};
#endif
#ifdef SSNM_cxx
SSNM::SSNM(TTree *tree) : fChain(0)
{
```

```cpp
        cout«"'Enter root file name:";
        cin»rootfile; // input file
        if (tree == 0) {
            TFile *f = (TFile*)gROOT->GetListOfFiles()->FindObject(rootfile);
            if (!f || !f− >IsOpen()) {
            f = new TFile(rootfile);}
            f->GetObject("MC_out",tree);
        }
        Init(tree);
}


SSNM::~̃SSNM()
{
if (!fChain) return;
delete fChain->GetCurrentFile();
}


Int_t SSNM::GetEntry(Long64_t entry)
{
// Read contents of entry.
if (!fChain) return 0;
return fChain->GetEntry(entry);
}


Long64_t SSNM::LoadTree(Long64_t entry)
{
// Set the environment to read one entry
        if (!fChain) return -5;
        Long64_t centry = fChain->LoadTree(entry);
        if (centry < 0) return centry;
        if (fChain->GetTreeNumber() != fCurrent)
        fCurrent = fChain->GetTreeNumber();
        Notify();
        }
        return centry;
}
void SSNM::Init(TTree *tree)
{
// Set branch addresses and branch pointers if (!tree) return;
fChain = tree;
fCurrent = -1;
```

```
fChain->SetMakeClass(1);
fChain->SetBranchAddress("eventID",&eventID,&b_eventID);
fChain->SetBranchAddress("stepID",&stepID,&b_stepID);
fChain->SetBranchAddress("trackID",&trackID,&b_trackID);
fChain->SetBranchAddress("parentID",&parentID,&b_parentID);
fChain->SetBranchAddress("kineticE",&kineticE,&b_kineticE);
fChain->SetBranchAddress("pE", &pE, &b_pE);
fChain->SetBranchAddress("x", &x, &b_x);
fChain->SetBranchAddress("y", &y, &b_y);
fChain->SetBranchAddress("z", &z, &b_z);
fChain->SetBranchAddress("postx", &postx, &b_postx);
fChain->SetBranchAddress("posty", &posty, &b_posty);
fChain->SetBranchAddress("postz", &postz, &b_postz);
fChain->SetBranchAddress("ptype",&ptype,&b_ptype);
fChain->SetBranchAddress("time",&time,&b_time);
fChain->SetBranchAddress("volumeName",&volumeName,&b_volumeName);
fChain->SetBranchAddress("pdgNum",&pdgNum,&b_pdgNum);
Notify();
}

Bool_t SSNM::Notify()
{
return kTRUE;
}

void SSNM::Show(Long64_t entry)
{ cout<<"show"<<endl;
// Print contents of entry.
// If entry is not specified, print current entry
if (!fChain) return;
fChain->Show(entry);
}

Int_t SSNM::Cut(Long64_t entry)
{
cout<<"cut"<<endl;
// This function may be called from Loop.
// returns 1 if entry is accepted.
// returns -1 otherwise.
return 1;
}
```

#endif


**SSNM.cpp:**

```cpp
#define SSNM_cxx
#include "SSNM.hh"
#include <iostream>
#include <fstream>
#include <TROOT.h>
#include <TStyle.h>
#include <TRint.h>
#include <TApplication.h>
#include <TFormula.h>
#include <TChain.h>
#include <TString.h>
#include <TF1.h>
#include <TH1.h>
#include <TH2.h>
#include <TH3.h>
#include <TFile.h>
#include <TMath.h>
#include <TCanvas.h>
#include <TString.h>
#include <TGraphErrors.h>
#include <TVector3.h>
#include <TLorentzVector.h>
#include <TDirectory.h>
#include <TLine.h>
#include <string>
#include <vector>
#include <deque>
#include <random>
#include <TRandom.h>
#ifdef __CINT__
#pragma link C++ class std::vector<int>;
#pragma link C++ class ADAQRootMeasParams+;
#endif
using namespace std;
void Loop();
void doplots(int);
double energymap[46][21];
```

```cpp
double countmap[46][21];

int main(int argc, char** argv)
{
//set style and color scheme for root
gROOT->SetStyle("Plain");
gStyle->SetPalette(1);
SSNM pass1;
cout<<"Starting to perform analysis"<<endl;
pass1.Loop();
cout<<"Analysis has finished"<<endl;
}

void SSNM::Loop()
{
TFile *graphs;
graphs = new TFile("Results_Cf5E8.root""recreate");//Output file
int event_flag=0;
int event_number=-1;
int track_flag=0;
int track_number=-1;
int count_1=0;
double energy_deposit_event=0.;
double energy_deposit_Li=0.;
double energy_deposit_pvt_event=0.;
double energy_deposit_Li_event=0.;
double energy_deposit_Li_event_scatter=0.;
double energy_deposit_PVT_event_scatter=0.;
double energy_deposit_Li_event_q=0.;
double energy_neutron=0;
double energy_previous_neutron=0;
double calculated_deltaE_neutron=0;
double rad_pos = 0.;
double rad_pos_post=0.;
double time_t=0.; //thermalization time
double time_c=0.; //capture time
double distance_t=0.; //thermalization distance
double distance_c=0.; //capture distance
double FirstScatterEnergyLossRatio=0;
double InitialNeutronEnergy=0;
double count_nothermalbutcapture=0;
```

```cpp
double FWHM_PVT=0;
double capturemoment=0;
int Count_H=0;
int Count_C=0;
int Count_Hnumber=0;
int Count_Cnumber=0;
int tflag=0;
int cflag=0;
int PVT_scatter_flag=0;
int ii=0;
int jj=0;
deque<int> Nb_Collisions;
deque<string> Recoil;

TH1F *energy_hist;
energy_hist = new TH1F("energy","Energy;Energy (MeV);Counts",3000,0.,30.);

TH1F *timether_hist;
timether_hist = new TH1F("time_thermal","ThermalTime;Time (us);Counts",200,0.,20.);

TH1F *timecapt_hist;
timecapt_hist = new TH1F("time_capture","Capture Time;Time (us);Counts",200,0.,20.);

TH1F *disttherm_hist;
disttherm_hist = new TH1F("dist_ther","D to Thermalize;Distance (mm);Counts",300,0.,300.);

TH1F *distcaputre_hist;
distcaputre_hist = new TH1F("dist_capture","D to Capture;Distance (mm);Counts",250,0.,250.);

TH1F *energy_hist_PVT;
energy_hist_PVT = new TH1F("energy_PVT","E_PVT;Energy(MeV);Counts",3000,0.,30.);

TH1F *energy_hist_glass;
energy_hist_glass = new TH1F("energy_glas","E_glass;Energy(MeV);Counts",3000,0.,30.);

Collision_hist = new TH1F("Collision_hist","Nb of collisions before capture; Nb of collisions;
Counts",50,0.,50.);

TH1F *H_EnergyRatio_hist = new TH1F("H_EnergyRatio_hist","Energy loss ratio; Energy
loss ratio; Count",100,0.,1.);
```

```
TH1F *C_EnergyRatio_hist = new TH1F("C_EnergyRatio_hist","Energy loss ratio; Energy
loss ratio; Counts",100,0.,1.);

TH1F *TotalEnergyLossRatioPVT_hist = new TH1F("TotalEnergyLossRatioPV_hist","Energy
loss ratio; Energy loss ratio; Count",1000,0.,1.);

TH1F *TotalEnergyLossRatioGlass_hist = new TH1F("TotalEnergyLossRatioGlass_hist","Energy
loss ratio; Energy loss ratio; Counts",1000,0.,1.);

TH1F *TotalEnergyLossRatioTotal_hist = new TH1F("TotalEnergyLossRatioTotal_hist","Energy
loss ratio; Energy loss ratio; Counts",1000,0.,1.);

TH1F *CaptureEnergy_hist = new TH1F("CaptureEnergy_hist","Neutron energy at capture;
Neutron energy at capture",2000,0.,10);

TH1F *NEnergyCapNoHCcollision_hist=new TH1F("NEnergyCapNoHCcollision_hist","Counts;
Neutron energy (MeV)", 1000,0,10);

TH1F*CapturedIncidentE_hist=new TH1F("CapturedIncidentE_hist","Counts; Neutron en-
ergy (MeV)", 1000,0,10);

TH2F*CollisionSequence_hist=new TH2F("CollisionSequence_hist","CollisionSequence_hist; Nb
of Collisions with hydrogen atoms; Nb of Collisions with carbon atoms", 45,0,45,20,0,20);

TH2F*CollisionEnergyDeposition_hist=new TH2F("CollisionEnergyDeposition_hist",
"CollisionEnergyDeposition_hist; Nb of Collisions with hydrogen atoms; Nb of Collisions with
carbon atoms", 45,0,45,20,0,20);

for (ii=0; ii<45;ii++) {
    for (jj=0; jj<20;jj++) {
    energymap[ii][jj]=0;
    countmap[ii][jj]=0;
    }
}

if (fChain == 0) return;
Long64_t nentries = fChain->GetEntriesFast();
Long64_t nbytes = 0, nb = 0;
for (Long64_t jentry=0; jentry<nentries;jentry++) {
Long64_t ientry = LoadTree(jentry);
if (ientry < 0) break;
```

```
nb = fChain->GetEntry(jentry); nbytes += nb;
//check to see if particle is in the detector
rad_pos=sqrt(pow(x,2.)+pow(y,2.));
rad_pos_post=sqrt(pow(postx,2.)+pow(posty,2.));
// if(rad_pos>127.||z>38.) continue;
// if(rad_pos_post>127.||postz>38.) continue;

//first check events
if(event_number==-1) {
event_number=eventID;
InitialNeutronEnergy=kineticE;
}

if(event_number!=eventID)
if(energy_deposit_event>0.) energy_hist->Fill(energy_deposit_event/1000.);
if(energy_deposit_pvt_event>0.) energy_hist_PVT->Fill(energy_deposit_pvt_event/1000.);
if(energy_deposit_Li_event>0.) energy_hist_glass->Fill(energy_deposit_Li_event/1000.);
if (energy_deposit_pvt_event>0) {
// Collision_hist->Fill(Recoil.size());
}

if (cflag==1) { CollisionSequence_hist->Fill(Count_Hnumber,Count_Cnumber);
if ((Count_Cnumber<21) && (Count_Hnumber<46)){
countmap[Count_Hnumber][Count_Cnumber]=countmap[Count_Hnumber][Count_Cnumber]+1;
energymap[Count_Hnumber][Count_Cnumber]=energymap[Count_Hnumber][Count_Cnumber]+
energy_deposit_PVT_event_scatter/InitialNeutronEnergy;
}

CaptureEnergy_hist->Fill(energy_neutron);
CapturedIncidentE_hist->Fill(InitialNeutronEnergy/1000);

if (energy_deposit_PVT_event_scatter/InitialNeutronEnergy<1) {
    TotalEnergyLossRatioPVT_hist->
    Fill(energy_deposit_PVT_event_scatter/InitialNeutronEnergy);
} else {TotalEnergyLossRatioPVT_hist->Fill(1.00);}

if (energy_deposit_Li_event_scatter/InitialNeutronEnergy<1) {
    TotalEnergyLossRatioGlass_hist->Fill(energy_deposit_Li_event_scatter/
    InitialNeutronEnergy);
} else { TotalEnergyLossRatioGlass_hist->Fill(1.00);}
```

```
if ((energy_deposit_PVT_event_scatter+energy_deposit_Li_event_scatter)
/InitialNeutronEnergy<1) {
        TotalEnergyLossRatioTotal_hist->Fill
        ((energy_deposit_PVT_event_scatter+energy_deposit_Li_event_scatter)
        /InitialNeutronEnergy);
} else { TotalEnergyLossRatioTotal_hist->Fill(1.00);}

Nb_Collisions.push_back(Recoil.size());
Collision_hist->Fill(Recoil.size());
if (energy_deposit_PVT_event_scatter==0) {
        NEnergyCapNoHCcollision_hist->Fill(InitialNeutronEnergy/1000);
}

if (Recoil.size()<1) {
        count_1=count_1+1;
}

if ((Recoil.size()==1)&&(Recoil[0]=="proton")) {
        H_EnergyRatio_hist->Fill(FirstScatterEnergyLossRatio);
        Count_H=Count_H+1;
}

if ((Recoil.size()==1)&&((Recoil[0]=="C12")||(Recoil[0]=="C13")||(Recoil[0]=="C14"))) {
        C_EnergyRatio_hist->Fill(FirstScatterEnergyLossRatio);
        Count_C=Count_C+1;
}
Recoil.clear();

if (PVT_scatter_flag==0){
count_nothermalbutcapture=count_nothermalbutcapture+1;
}
} else {
Recoil.clear();
}
//reset everything and move to next event
event_number=eventID;

time_t=time; //thermalization time
time_c=0.; //capture time
distance_t=0.; //thermalization distance
distance_c=0.; //capture distance
```

```
tflag = 0;
cflag = 0;
energy_deposit_pvt_event=0.;
energy_deposit_PVT_event_scatter=0.;
energy_deposit_Li_event=0.;
energy_deposit_event=0.;
energy_deposit_Li_event_scatter=0.;
track_flag=0;
track_number=trackID;
PVT_scatter_flag=0;
energy_deposit_gamma=0;
energy_deposit_gamma_smear=0;
InitialNeutronEnergy=kineticE;
Count_Hnumber=0;
Count_Cnumber=0;
}

if(track_number==-1){
track_number=trackID;
}

if((track_number!=trackID)&&(event_number==eventID)){
track_flag=1;
}

if (volumeName=="PVT_Scint") {
     energy_deposit_pvt_event+=pE;
     if(((ptype=="proton")||(ptype=="deuteron")||(ptype=="C12")||
     (ptype=="C13")|| (ptype=="C14"))&&(time<capturemoment)){
         PVT_scatter_flag=1;
         energy_deposit_PVT_event_scatter+=pE;
     }
}

if(volumeName=="LiG_Scint"){ //volume must be Lithium glass
     if(ptype=="triton"||ptype=="alpha"){ //if it is a triton or alpha
     pE=pE*(1.5/4.8);
     }
     else {
     if (time<capturemoment) {
         energy_deposit_Li_event_scatter+=pE;
```

```
        }
        }
energy_deposit_Li+=pE;
energy_deposit_Li_event+=pE;
}

if(parentID==0&&kineticE<0.000025&&ptype=="neutron"){
        distance_t+=sqrt(pow(postx-x,2.)+pow(posty-y,2.)+pow(postz-z,2.));
}

if(ptype=="neutron") {
        if (stepID==1) {
        energy_previous_neutron=kineticE;
        }
energy_neutron=kineticE;
calculated_deltaE_neutron=energy_previous_neutron-energy_neutron;
energy_previous_neutron=kineticE;
}

if(ptype=="neutron"&&kineticE<0.000025&&parentID==0&&tflag==0){
        disttherm_hist->Fill(distance_t);
        timether_hist->Fill(time-time_t);
        tflag=1;
}

if(volumeName=="LiG_Scint"){
        if(ptype=="triton"&& cflag==0){
        distcaputre_hist->Fill(distance_t);
        timecapt_hist->Fill(time-time_t);
        cflag=1;
        capturemoment=time;
        }
}
energy_deposit_event+=pE;

if(volumeName=="PVT_Scint"){
if( ((ptype=="proton")|| (ptype=="deuteron")||||(ptype=="C12")|| (ptype=="C13")
|| (ptype=="C14"))&&(track_flag==1)&&(time<capturemoment)){
        FirstScatterEnergyLossRatio=kineticE/InitialNeutronEnergy;
        track_flag=0;
        Recoil.push_front(ptype);
```

```
            if((ptype=="proton")||(ptype=="deuteron")) {
            Count_Hnumber+=1;
            }
            if((ptype=="C12")||(ptype=="C13")||(ptype=="C14")){
            Count_Cnumber+=1; }
        }
}
track_number=trackID;
}

for (ii=0; ii<45;ii++) {
      for (jj=0; jj<20;jj++) {
            if (countmap[ii][jj]>0) {
            energymap[ii][jj]=energymap[ii][jj]/countmap[ii][jj];
            CollisionEnergyDeposition_hist->Fill(ii,jj,energymap[ii][jj]);
            }
      }
}
graphs->Write();
graphs->Close();
}
```